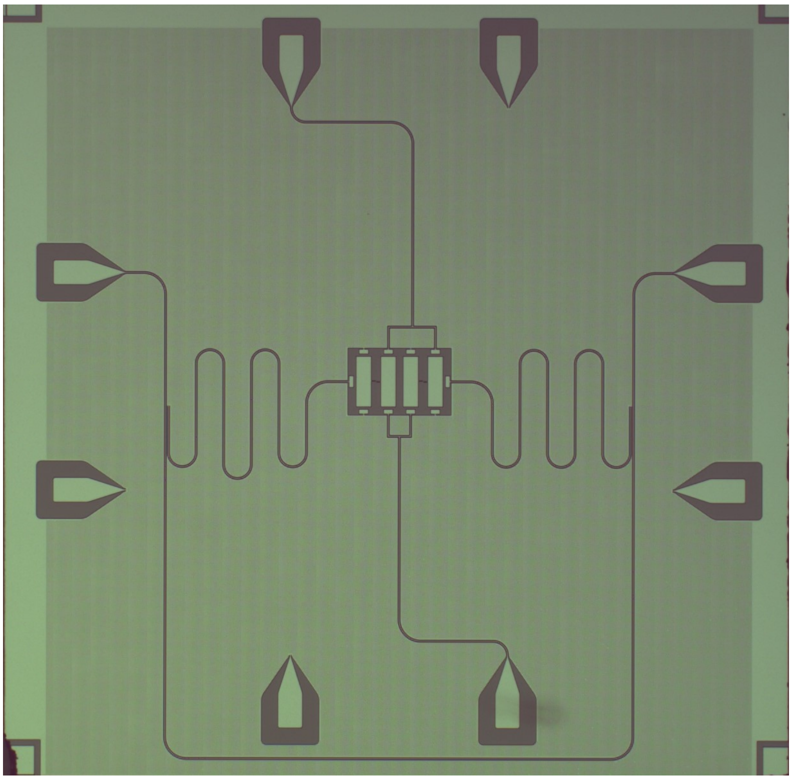

# Engineering decay rates of Hybridised modes in Superconducting circuits

Master thesis in Erasmus Mundus Masters in Nanoscience and Nanotechnology

KOWSHIK ERAPPAJI PATEL

Promoter: Asst. Prof. Simone Gasparinatti

Co-promoter: Prof. Bart Soree

Department of Microtechnology and Nanosciece
Chalmers University of Technology
Gothenburg, Sweden 2020

Funded by the
Erasmus+ Programme
of the European Union

Master's thesis in Erasmus Mundus Masters in
Nanoscience and Nanotechnology

# Engineering decay rates of Hybridised modes in Superconducting circuits

Kowshik Erappaji Patel

Department of Microtechnology and Nanoscience
*Quantum Technology Laboratory*
Chalmers University of Technology
Gothenburg, Sweden 2020

Engineering decay rates of Hybridised modes in Superconducting circuits

Kowshik Erappaji Patel

Supervisor: Asst. Prof. Simone Gasparinatti, Department of Microtechnology and Nanoscience

Master's thesis in Erasmus Mundus Masters in Nanoscience and Nanotechnology
Department of Microtechnology and Nanoscience
Quantum Technologies Laboratory
Chalmers University of Technology
SE-412 96 Gothenburg

Cover: An optical micrograph of the sample designed to study the decay rates of hybridised modes.

Chalmers Reproservice
Gothenburg, Sweden 2020

Engineering decay rates of Hybridised modes in Superconducting circuits
Master's thesis in Erasmus Mundus Masters in Nanoscience and Nanotechnology

KOWSHIK ERAPPAJI PATEL
Department of Microtechnology and Nanoscience
Quantum Technologies Laboratory
Chalmers University of Technology

# Abstract

Recently, circuit Quantum Electrodynamics (cQED) has enabled study of light matter interaction in superconducting circuits. In this work, we study transitions from hybridized modes in a cQED architecture. We obtain hybridized modes from degenerate levels of capacitively coupled transmon qubits. We collectively couple the qubits to two microwave waveguides, so that each hybridized mode selectively decays into one of the waveguides. We design this quantum circuit by using electrostatic and lumped-element simulations. To test the design, we perform microwave spectroscopy measurements of a nanofabricated sample cooled down in a dilution refrigerator. Our measurements confirm that the two hybridized modes respond as effective two-level systems, each strongly coupled to a different waveguide. This arrangement could be used to explore heat transfer between waveguides, mediated by a quantum system, paving the way for experiments in quantum thermodynamics.

Keywords: Hybridised modes, Resonance fluroscence, Quantum thermodynamics, Circuit QED.

# Acknowledgements

I would like to thank Simone Gasparinatti for giving me the opportunity to work on this project. A heartfelt gratitude for all the support, knowledge and guidance received during the past year. I would also like to thank Marco Scigliuzzo for all the help received during fabrication, conduction of experiment. I would like to thank Daniel Perez and Amr Osman for the fabrication of the two designs with which the experiments in this work were conducted. I would like to thank Marina Kudra, Christian Krizan, and Yong Lu for useful discussion and guidance.
I would like to thank Bart Soree and Thilo Bauch for giving me an opportunity pursue EMM Nano masters program. I would like to thank all my friends and family for the support received during the masters.

KOWSHIK ERAPPAJI PATEL, Gothenburg, Aug 2020

# Contents

# List of Figures

# List of Tables

# 1

# Introduction

Maxwell's demon [3] and the single-particle thought experiment of Szilard [4] seemingly violated the second law of thermodynamics. This lead to equivalency between information and entropic degrees of freedom, in the form of Landauer's principle [5]. At the same time, the advancements in information processing have lead to a search for new paradigms of computing, and quantum information processing [6] has emerged to solve certain problems faster than classical computers. The advantage in speed up of information processing makes us investigate heat transport processes, as to if there is a quantum advantage. It is necessary to understand, if engines and refrigerators made at the nanoscale show an advantage and if quantum coherences have a role to play in them.

The ability to trap and control single particle like electron or an atom has lead to the implementation of many thought experiments. Landauer's principle has been demonstrated in a colloidal double potential well [7]. Extraction of heat from Szilard engine cycle using a single electron transistor has also been demonstrated [8]. There are proposals to investigate measurement-assisted cooling and nonequilibrium fluctuations in quantum system acting as heat engines or refrigerators [9],[1].

In the last 15 years, great progress on the measurement and control of individual quantum systems has been achieved in an architecture called circuit quantum electrodynamics (cQED). In cQED, superconducting circuits including resonators and "artificial atoms" based on Josephson junctions are cooled down to very low temperatures (<100mK) and addressed using microwave signals. This architecture was recently exploited in Google's landmark experiment claiming "quantum supremacy" using a quantum processor consisting of 53 bits [10]. This architecture could lend itself well to studies of quantum thermodynamics, too. However, only a limited number of experiments have been so far performed in this direction [11, 12, 13], and the search for a genuine quantum advantage in thermodynamics is still open.

In this MSc thesis work, we take the first steps towards realizing a cQED system that is amenable to implement the quantum measurement cooling concept described in Ref. [1]. The proposed protocol comprises two qubits and two heat baths held at different temperatures. Each qubit can be coupled to a single heat bath, and the two qubits can be entangled. A cooling cycle consisting of thermalization, entanglement, and measurement of an individual qubit is used to extract work from a bath and transfer it to the another bath at higher temperature, thereby achieving cooling. The proposal also suggests that efficiency of heat extraction is maximized when the two qubits are maximally entangled.

In our realization of the proposal, we design an analog quantum circuit in which quantum measurement cooling can be achieved with continuous operations. The two qubits are resonant and strongly coupled to each other, so that they fully hybridize and form a symmetric and antisymmetric mode. Using circuit symmetries, we engineer the decay of the composite qubit system into two waveguides, so that each mode predominantly decays into a selected waveguide. In addition, we couple each qubit to a readout resonator, so that it can be measured with a variable strength by driving the resonator with a coherent tone of given amplitude. A projective measurement of one of the qubits randomizes its phase; in the hybridized based, this leads to an equalization of the populations of the hybridized modes. This, in combination with the engineered decay rates, can activate an energy transfer between the two waveguides. In this thesis, we present the concept, design, implementation, and characterization of the device. In particular, we use power-dependent spectroscopy measurements to verify that each of the hybridized modes is strongly coupled to the intended waveguide, to which it primarily decays. The demonstration of measurement-activated heat transfer is left for future studies.

This master thesis is organized into four chapters. In the second chapter, the background needed to understand this work is discussed. The simulation related to designing the quantum circuit is discussed in the third chapter. In the fourth chapter, the results from the experiments are presented.

# 2

# Background

This chapter includes description of theoretical background required to understand the experiments and results of this thesis. In the first a brief introduction about Circuit QED and its different elements are discussed, like a transmon qubit and coplanar waveguide resonators. Coherent scattering between waveguides and qubits follows the explanation about qubits and resonators. The description of the concept of the experiment is explained in the last section of this chapter.

## 2.1 Circuit Quantum Electrodynamics

Circuit QED is the study of quantum optics using artificial atom made up of superconducting qubits and transmission line resonators. The equivalency between artificial atoms coupled to resonators, and atoms coupled to optical cavities, allows one to use concepts of quantum optics to describe these systems. Simulation of complex quantum systems using circuits has lead to increased interest in Circuit QED. The implementation of error correction and various multiplexing techniques in Circuit QED makes it a suitable choice for scalable quantum computing [14, 15].

### 2.1.1 Transmon Qubit

An artificial atom is made from systems having a well like potential also has discrete energy levels. One such system involves a superconducting Josepshon junction. The overlap of wavefunction of two superconducting electrodes across an insulator/ normal metal forms a Josephson junction. Superconducting qubits are made using the non linear potential energy of a Josephson junction. Copper pair box was the first charge qubit [20] made with superconducting tunnel junction in between a gate electrode and a small metallic island. The Hamiltonian of a charge qubit is given by

$$\hat{H} = 4E_C(\hat{n} - n_g) - E_J \cos\hat{\varphi} \tag{2.1}$$

where $E_C$ and $E_J$ are analogous to the kinetic and potential energy, with $\hat{n}$ number operator for Cooper pairs on the island, $\hat{\varphi}$ phase difference across the junction, $n_g = (C_g V_g + Q_r)/2e$, charge on the gate island in units of Cooper pairs; charging energy

$$E_C = e^2/2C_\Sigma, \tag{2.2}$$

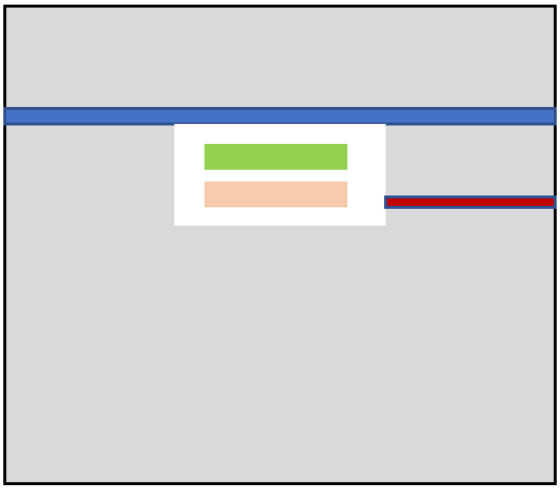

**Figure 2.1:** *Layout of Transmon Qubit showing the two qubit islands, the drive and the read out waveguide (Grey: Ground plane, Blue: waveguide, Red: Resonator, Green and yellow: qubit islands).*

where $C_\Sigma = C_{JJ} + C_g$ ; $e$ is the elementary charge, and $E_J = \Phi_0 I_c/2\pi$ is the Josephson energy ($\Phi_0$ is the flux quantum and $I_c$ is the critical current of the Josephson Junction).

One of the dominant decoherence mechanism in a Cooper Pair Box qubit is charge sensitivity noise. This is caused due disturbances in the charge on the gate island. Energy of a $m^{th}$ level $E_m$ and energy separation $E_{m1m2}$ is dependent on the charge on the island in both Copper pair box and transmon configuration. Variations of charge cause first order corrections (of $n_g$) to the energy levels that can be modeled by $\epsilon_m$, the peak to peak value of energy dispersion of $m^{th}$ level. This can be to some extent mitigated by operating the qubit in a 'sweet spot' close to the charge degeneracy point [21] as there is no variation of energy at this point ($\frac{\partial E_m}{\partial n_g} = 0$). In the transmon configuration [16], charge sensitivity noise is resolved by adding a large shunt capacitance in which the charge dispersion has a relation

$$\epsilon_m = (-1)^m E_C \frac{2^{4m+5}}{m!} \sqrt{\frac{2}{\pi}} (\frac{E_J}{2E_C})^{\frac{m}{2}+\frac{3}{4}} e^{-\sqrt{8E_J/E_C}} \tag{2.3}$$

.

The total energy separation (for first two levels) has a dispersion relation

$$\epsilon = E_C \sqrt{\frac{2}{\pi}} e^{-\sqrt{8E_J/E_C}} (2^5 (\frac{E_J}{2E_C}) - 2^9 (\frac{E_J}{2E_C})) \tag{2.4}$$

By choosing values for $E_J/E_C$ one can exponentially reduce the charge sensitivity noise of the qubit. For decoherence times in the microsecond range the $E_J/E_C$ can be in the order of hundred. While designing a qubit, targeted transition frequency is fixed and by referring to the graph Fig. 2.2 for a preferred noise level the charging energy is chosen and then the corresponding Josephson energy is calculated (2.5). By choosing a larger capacitive islands, lower charging energy and lesser noise can be obtained. The resolution and reliability of the fabrication process also limits the exact Josephson energy as the size of the junction is related to its critical current.

$$\hbar\omega_{ge} = \sqrt{8E_J E_C} - E_C \tag{2.5}$$

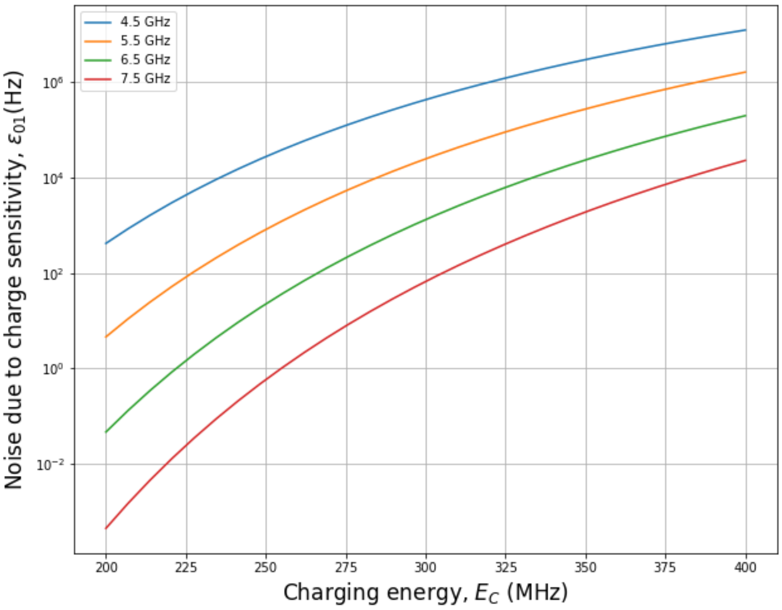

**Figure 2.2:** *Charge insensitivity noise equivalent frequency as a variation of charging energy for different transition frequency of a transmon qubit*

### 2.1.2 Coplanar Waveguide and Transmission line resonator

Coplanar waveguide (CPW) is a transmission line composed of 3 conductors, of which 2 return lines (ground) separated with a gap from a central conductor on a dielectric substrate. Such coplanar waveguides when shorted/grounded at their ends, host a discrete set of modes, equivalent to a cavity in CQED. Boundary conditions of the waveguide result in 2 different types of resonators, a $\lambda/2$ resonator, and a $\lambda/4$ resonator. As the name suggest either a half wavelength or a quarter wavelength of a resonant electromagnetic field respectively. CPW resonators act as a cavity for microwave radiation.

Resonators can be coupled to the transmission line either capacitively or inductively depending on the boundary conditions. Transmission lines act as drive and output lines for the resonator. The Notch configuration of a $\lambda/4$ resonator is obtained by coupling it to a transmission line (Fig. 2.3(c)).

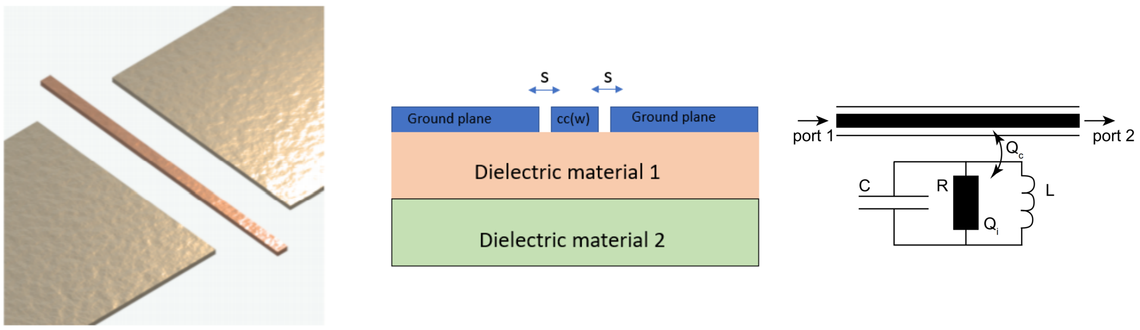

**(a)** **(b)** **(c)**

**Figure 2.3:** *(a) Top view of coplanar waveguide showing the metalization of lateral ground plane and central conductor (cc)[17]. (b) Side view of coplanar waveguide resonator [18].(c) Notch configuration showing a RLC oscillator coupled to a transmission line. [23]*

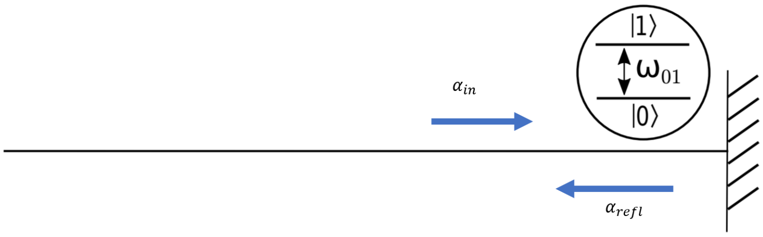

**Figure 2.4:** *A transmission line to which a qubit is coupled at its end. The coherent incident signal is $\alpha_{in}$ and the signal reflected from mirror is $\alpha_r efl$*

### 2.1.3 Coherent scattering from a two level system

When a resonant electromagnetic field is incident on atom, the atom gets excited and re-emits the absorbed photons. Light may be scattered coherently or incoherently by the atom. Coherent scattered light has zero relative phase, while incoherently scattered light have random phase. When such a scattering experiments is conducted with atom it is difficult to have the atom emit into a single mode. But when an artificial atom is coupled to a transmission line (2.4 ), its emission can be dominated by decay into it. The steady state analysis of system of artificial atom with internal losses coupled to a transmission line results in equation below for the reflection coefficient of the transmission line:

$$r = 1 - \frac{2\Gamma(\Gamma + \Gamma_{nr} + 2i\Delta)}{\Gamma^2 + \Gamma\Gamma_{nr} + \Gamma_{nr}^2 + 4\Delta^2 + 2\Omega_P^2} \tag{2.6}$$

where $\Gamma$ is coupling between the qubit and the transmission line, $\Gamma_{nr}$ is the loss rate in the qubit, $\Delta = \omega$-$\omega_{ge}$ is the frequency detuning from the fundamental transition, and $\Omega_P$ is the amplitude of the driving Rabi frequency.

If a coherent drive signal is incident on a waveguide coupled to a qubit either the signal can be reflected from the mirror or interact with qubit. In the interaction the resonant signal will be absorbed and reemitted from the qubit. In microwave

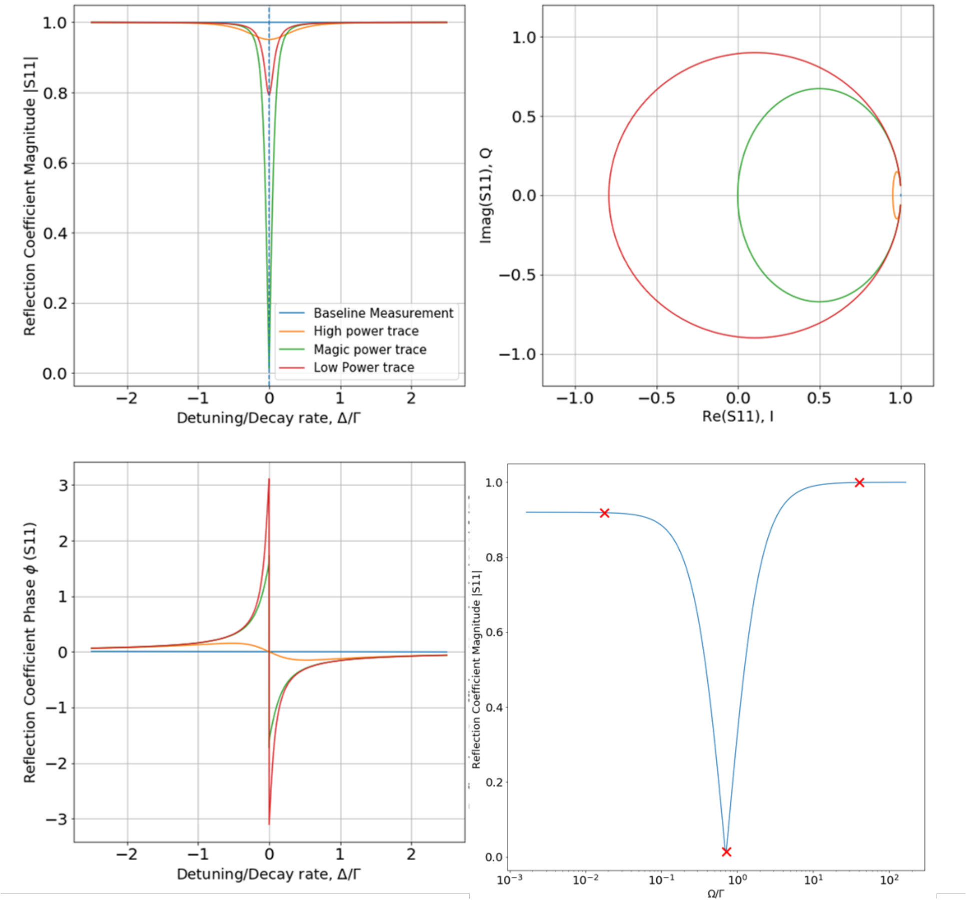

**Figure 2.5:** *The reflection coefficient from an artificial atom in magnitude, phase and IQ plane with decreasing drive power. A line cut of magnitude of reflection coefficient at different drive power is also shown*

domain such measurements are recorded using reflection coefficients S11 $= \alpha_{out}/\alpha_{in}$. S11 is a complex valued coefficient and can be studied using its magnitude, phase and IQ plane which is real value of S11 plotted against imaginary value of S11. S11 from reflection spectroscopy of waveguide coupled to qubit is shown in Fig. 2.5. Unlike a linear resonator the non linear qubit response is dependent on the input power Fig.2.5(d). At high power ($\Omega_p > 16\Gamma$) the qubit is saturated and all the incident signal is reflected but the mirror. At Rabi amplitude $\Gamma/\sqrt{2}<\Omega<16\ \Gamma$ there is loerntzian dip in the magnitude close to resonance frequency and a small phase change. When $\Omega_p$=$\Gamma/2$ at resonance point there is complete destructive interference of the incident and re-emitted signal from the qubit which has a $\pi$ phase change. When the input is such that $\Omega_p$<$0.04\Gamma$, the information is in the phase of the signal. S11 undergoes a $\pi$ phase change at resonance at these lower frequencies.

## 2.2 Concept of the experiment

Level diagram Fig.2.6 captures the idea of the experiment. Considering composite system of two capacitively coupled qubits degenerate states hybridise forming sym-

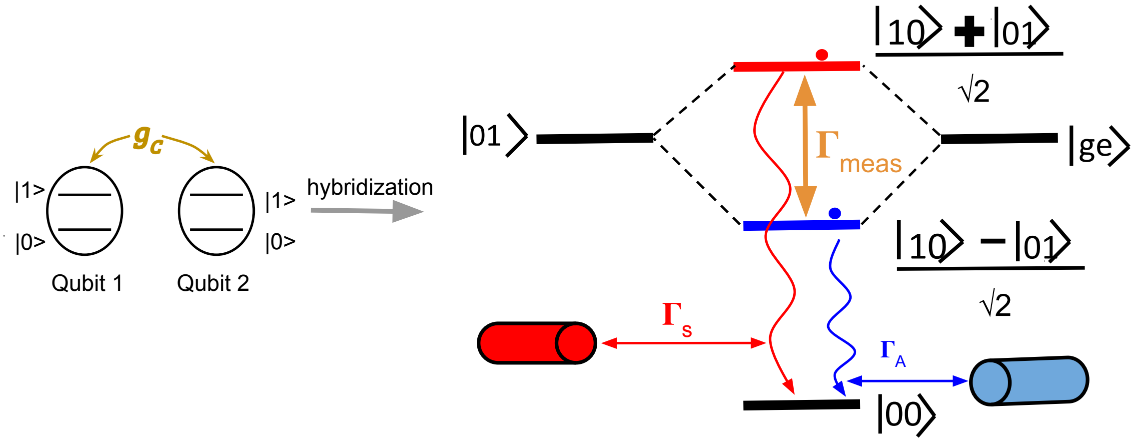

**Figure 2.6:** *(a)Level diagram of the composite qubit system. The two qubits, resonant and coupled with strength $g_c$, hybridize to form symmetric and antisymmetric modes, $|ge\rangle \pm |eg\rangle$. The symmetric (antisymmetric) mode decays into the ground state with rate $\Gamma_S$ ($\Gamma_A$) by emitting a photon into the "hot" bath, H ("cold" bath, C).*

metric and antisymmetric mode. Symmetric mode wavefunction, upon interchanging the states of qubits 1 and 2 gives back the same wavefunction therefore called symmetric mode. Upon interchanging the states of qubit 1 and 2, the antisymmetric wavefunction picks up a negative sign hence antisymmetric. If the transitions from these hybridised mode is coupled to waveguide which has continuum of propagating modes, it can act as heat baths. The study of heat transfer by exchanging photons between the waveguides mediated by the hybridised levels means that quantum coherence is affecting the heat flow of between the baths. One of the ways exchange of photons would transfer heat is by measuring the qubits in single qubit basis. This would also require that hybridised mode couple deferentially to two different waveguide. That is ideally, symmetric mode couples only to a symmetric waveguide while the antisymmetric mode couples to a antisymmetric waveguide. This is a challenge in itself. In this work this is partially achieved by circuitQED in an analog quantum system.

In the composite system, the symmetric mode couples strongly to a symmetric waveguide and weakly to the antisymmetric waveguide. The antisymmetric mode couples strongly to the antisymmetric waveguide and weakly to the symmetric waveguide. Measurement based dephasing of qubit would equalize the population of symmetric and antisymmetric mode enabling photon exchange between the symmetric and antisymmetric waveguide. This is equivalent to exchanging photons between hot bath (symmetric waveguide) and cold bath (antisymmetric waveguide). An optimized circuit design should have very low coupling between symmetric (antisymmetric) mode and antisymmetric (symmetric) waveguide.

In the discussions following this text symmetric mode which is superposition of degenerates states $|ge\rangle$ and $|eg\rangle$, $((|ge\rangle + |eg\rangle)/\sqrt{2})$ would be represented by +. Antisymmetric mode $((|ge\rangle - |eg\rangle)/\sqrt{2})$ would be represented by -. The waveguides would be noted by A(S) for Antisymmetric (Symmetric) waveguide.

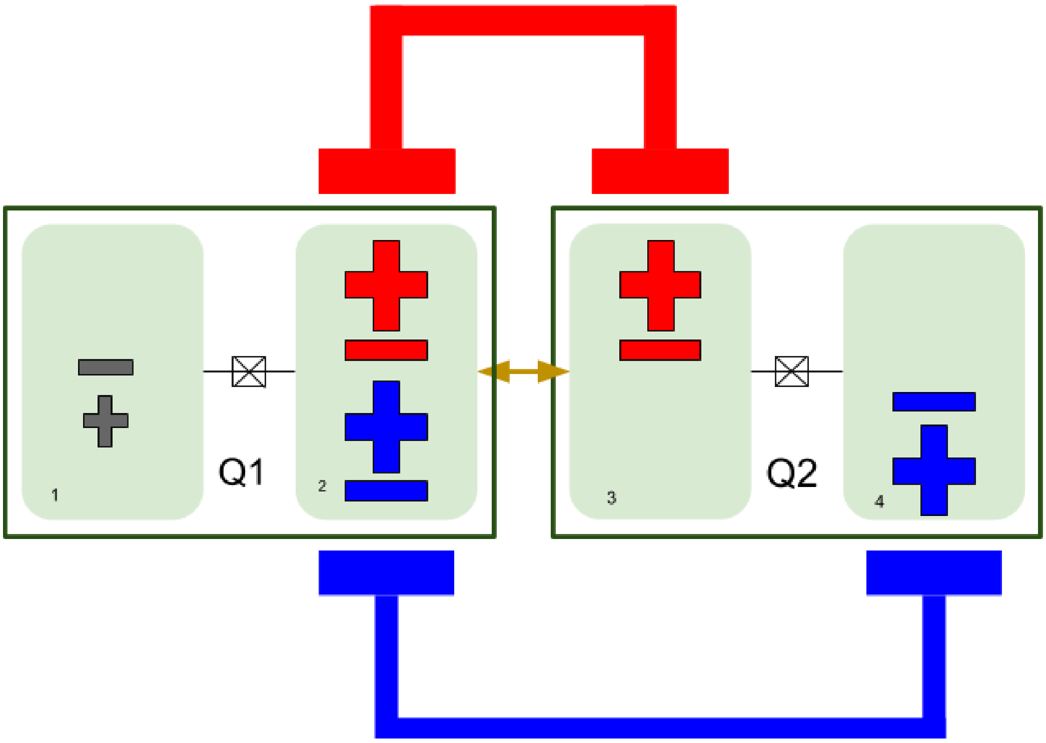

**Figure 2.7:** *Sketch of the circuit implementing the engineered decay rates of panel (a). Red: Symmetric waveguide, Blue: Antisymmetric waveguide, Green: qubit islands, Crosses: Josephson junctions. The relative phase of the excitations for the two modes is indicated by plus/minus signs. Constructive/destructive interference at the coupling points determines the enhancement/suppression of the coupling to the waveguides.*

The quantum circuit which implements this system is shown in Fig.2.7. It shows two transmon qubits represented by four green islands with Josephson junction. The qubits are identical having the same transition energy, charging energy and Josephson energy. The qubits are capacitively coupled leading to hybridisation forming + and -. The S painted red in layout and A painted blue. The islands which form the qubits have voltage vacuum fluctuations. Of the two different islands that form a qubit these fluctuations are opposite in polarity. The waveguides by design enhance the fluctuations of voltage fluctuations of the islands that they are coupled to. That is S enhances the fluctuations of similar polarity between the islands 2 and 3. The A enhances the fluctuations of opposite polarities on the islands 2 and 4. The enhancement is due to the constructive interference of these fluctuations at the meeting point of the two arms of the waveguide. The coupling between + (-) and S (A) is $\Gamma_S$ ($\Gamma_A$). Cooling will be determined by an interplay between the measurement based dephasing-rate, $\Gamma_M$, and the coupling rates $\Gamma_S$ and $\Gamma_A$. Therefore, it is necessary to design and characterize the coupling rate between the modes and the waveguide. Other unintended relaxation channels are due to spurious coupling between waveguides and islands and to the intrinsic decay channels of the qubits. These relaxation channels will determine the internal quality factor of the modes, as determined in a reflection spectroscopy measurement. Finally, each qubit in our setup is dispersively coupled to resonators for read out. The resonators are coupled inductively to a common transmission line for multiplexed read out on the same line. This design was made into a layout and fabricated for characterizing the devices.

### 2.2.1 Second order transitions

Qubits when interacting with a weak drive in the single photon range act as linear circuits but are indeed non linear. The non linearity in a superconducting circuit is produced by the Josephson Junction. The anharmonicity in a coupled qubit circuit results in hybridisation of $|ee\rangle$, $|gf\rangle$, and $|fg\rangle$ states and these states also cause second order transitions. In a second order transitions the qubits de-excite by simultaneously emitting 2 photons. The frequency of all the different transitions can be determined by solving for eigenvalues of a Hamiltonian,

$$H = \begin{pmatrix} \alpha & \sqrt{2}g & 0 \\ \sqrt{2}g & 0 & \sqrt{2}g \\ 0 & \sqrt{2}g & \alpha \end{pmatrix} \tag{2.7}$$

The eigenvalues of the above Hamiltonian is given by

$$E_1/\hbar = \alpha \tag{2.8}$$

$$E_2/\hbar = \frac{1}{2}(\alpha - \sqrt{16g^2 + \alpha^2}) \tag{2.9}$$

$$E_3/\hbar = \frac{1}{2}(\alpha + \sqrt{16g^2 + \alpha^2}) \tag{2.10}$$

The second order transitions measured in the experiment was numerically verified to be at this frequency. This transition was observed when in measurement one of the waveguide S or A was left floating. Using the frequency of this transition one can determine the anharmonicity of the designed qubits.

$$\omega_{sc} = \omega_{ge} + 1/2(\alpha + \sqrt{16g^2 + \alpha^2}) \tag{2.11}$$

# 3

# Methods

This chapter describes the methods involved in circuit simulation and experimental procedure of this work. The first two sections describes the simulations, which estimate the parameters of the quantum circuit. The experimental setup and measurements are described in the last section.

## 3.1 Estimation of Coupling strength

To estimate the coupling between the qubits and the waveguides a full quantization of the circuit is required. In the following section a method using which the coupling can be estimated is described. The Lagrangian formalism for circuits uses the flux (charge) as the position (momentum) variable . The electrostatic energy in a capacitive network is

$$\mathcal{L} = \frac{1}{2}\dot{\mathbf{\Phi}}^{\mathbf{T}} \cdot \mathbf{C} \cdot \dot{\mathbf{\Phi}} \tag{3.1}$$

where, the **C** is the capacitance matrix between different nodes in the circuit. The diagonal elements in the capacitance matrix **C** represent the mass of a particular node while the off diagonal elements represent the coupling between the two nodes in the network. The conjugate momentum of flux is the charge which is determined by

$$\mathbf{q} = \frac{\partial \mathcal{L}}{\partial \dot{\mathbf{\Phi}}} = \mathbf{C} \cdot \dot{\mathbf{\Phi}}$$

Rewriting the (kinetic part of the) Lagrangian in the charge basis would result in

$$\mathcal{L} = \frac{1}{2}\mathbf{q}^{\mathbf{T}} \cdot (\mathbf{C}^{-\mathbf{1}}) \cdot \mathbf{q} \tag{3.2}$$

The diagonal elements of the capacitance matrix represents the total mass of the element while the off diagonal elements are the perturbative corrections. The above consideration will let us estimate the strength of coupling and masses just by analyzing the matrix.

$$\mathbf{C} = \mathbf{C_d} + \mathbf{C}_\delta \tag{3.3}$$

where $C_d$ contains only the diagonal elements while the off diagonals are present in $C_\delta$

$$\mathbf{C} = \mathbf{C_d}(\mathbf{1} + \mathbf{C_d^{-1}}\mathbf{C}_\delta) \tag{3.4}$$

Since the Lagrangian depends on the inverse of Capacitance matrix inverting (3.4)

$$\mathbf{C}^{\mathbf{-1}} = (\mathbf{1} + \mathbf{C}_{\mathbf{d}}^{\mathbf{-1}}\mathbf{C}_{\delta})^{\mathbf{-1}}\mathbf{C}_{\mathbf{d}}^{\mathbf{-1}} \tag{3.5}$$

In the limit $C_d$ is far greater than $C_\delta$ the above equation can be approximated by

$$\mathbf{C}^{\mathbf{-1}} = (\mathbf{1} - \mathbf{C}_{\mathbf{d}}^{\mathbf{-1}}\mathbf{C}_{\delta})\mathbf{C}_{\mathbf{d}}^{\mathbf{-1}} \tag{3.6}$$

The inverse hence can be written as

$$\mathbf{C}^{\mathbf{-1}} = \mathbf{C}_{\mathbf{d}}{}^{\mathbf{-1}} - (\mathbf{C}_{\mathbf{d}}{}^{\mathbf{-1}}\mathbf{C}_{\delta}\mathbf{C}_{\mathbf{d}}^{\mathbf{-1}}) \tag{3.7}$$

The correction term element is of the form $C_{ij}/(C_{ii}C_{jj})$. The charge operator can be written as a function of impedance

$$q_i = \frac{1}{\sqrt{2Z_i}}(a_i + a_i^\dagger) \tag{3.8}$$

where $Z_i$ is the characteristic impedance of the $i^{th}$ node with resonance frequency $\omega_i$=$1/\sqrt{L_iC_i}$. Further substituting correction term of Equation.3.7 in Equation.3.2 we can find the coupling between two capacitive elements as

$$g_{ij} = \frac{1}{2}\omega_i\omega_j\sqrt{Z_iZ_j}C_{ij} \tag{3.9}$$

## 3.2 Estimation of qubit parameters

The circuit schematic which was simulated in Maxwell is shown in Fig.3.1. As the waveguides S and A are coplanar the extra islands need to be which are wire bonded to the ground plane of the chip. Symmetric grounded island (SGI) is added in between the arms of the S waveguide while the Antisymmetric grounded island (AGI) is added between the arms of the A waveguide. Dummy couplers are added to the circuit to make the circuit spatially symmetric around the origin which is in between the two qubits.

The parameters of Josephson junction do not depend on the capacitance network of the circuit, meaning the Josephson energy can be determined using the properties of the junction alone. Also, the coupling strength between different elements is dependant on the capacitance network without the junction. This allows us to calculate the charging energy of qubits and their couplings using electrostatic simulation in ANSYS Maxwell. The procedure of arriving at the design of the circuit is to obtain the capacitance matrix and calculate the charging energy. Use the capacitance values from the capacitance matrix in the circuit in AWR office and obtain the coupling between the two qubits. Further discussion will be based capacitance matrix given in Table.3.1.

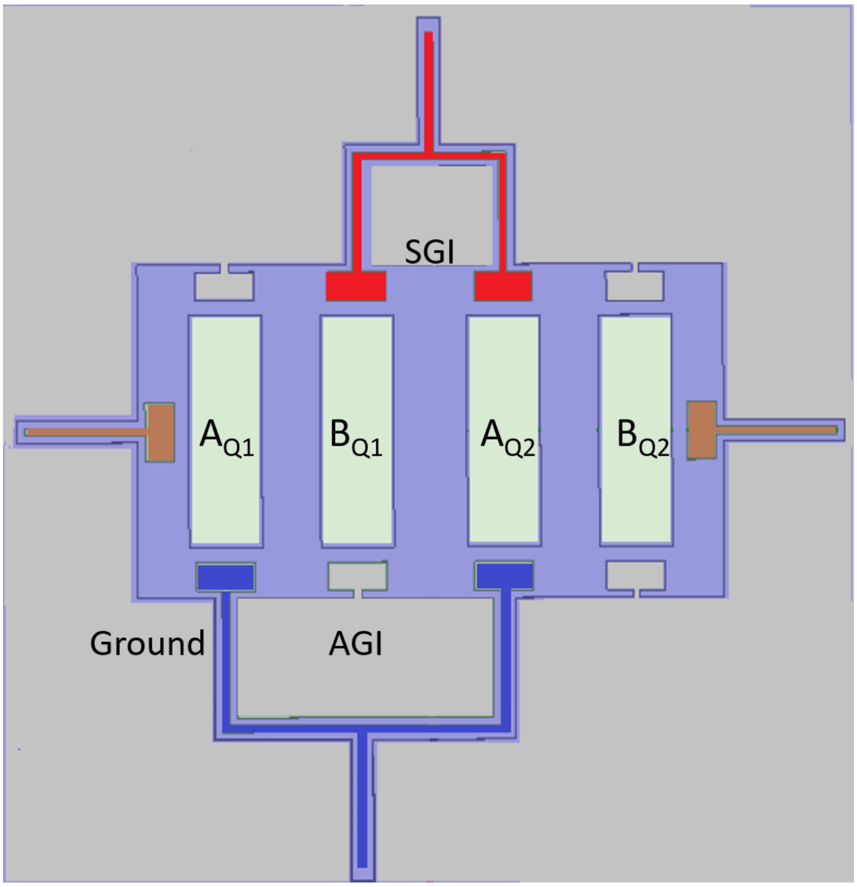

**Figure 3.1:** *Layout simulated in Maxwell showing the four metals ($A_{Q1}$, $B_{Q1}$, $A_{Q2}$, $B_{Q2}$) of the qubit, the S and A waveguide shown in red and blue respectively, resonators and SGI and AGI. Ground is denoted by grey and light blue denotes the substrate.*

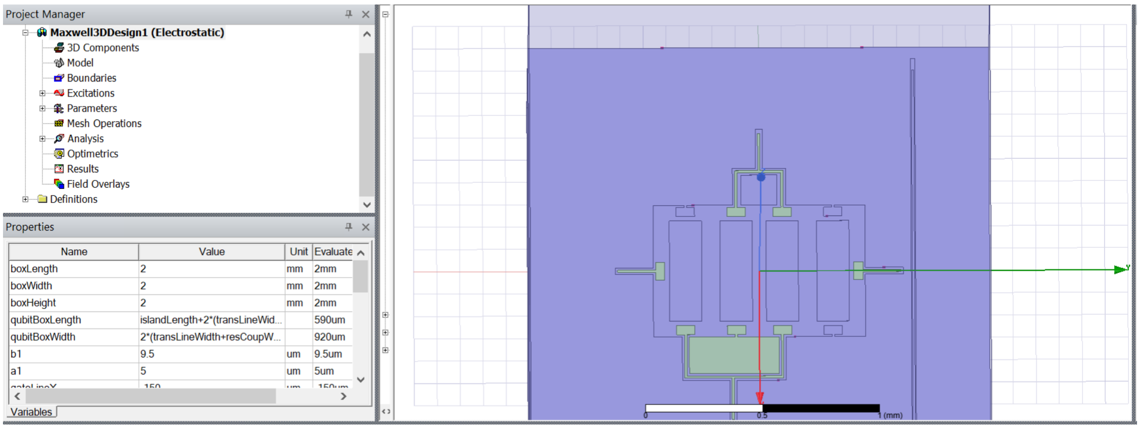

| Name | Value | Unit | Evaluate |
|---|---|---|---|
| boxLength | 2 | mm | 2mm |
| boxWidth | 2 | mm | 2mm |
| boxHeight | 2 | mm | 2mm |
| qubitBoxLength | islandLength+2*(transLineWid... |  | 590um |
| qubitBoxWidth | 2*(transLineWidth+resCoupW... |  | 920um |
| b1 | 9.5 | um | 9.5um |
| a1 | 5 | um | 5um |

**Figure 3.2:** *Snapshot of the ANSYS Maxwell software showing the design, variables and the properties of the design*

| | $A_{Q1}$ | $B_{Q1}$ | $A_{Q2}$ | $B_{Q2}$ | A | S | Ground |
|---|---|---|---|---|---|---|---|
| $A_{Q1}$ | 114 | 21.101 | 2.393 | 0.795 | 8.734 | 1.165 | 67.797 |
| $B_{Q1}$ | 21.101 | 110.73 | 25.745 | 2.379 | 2.100 | 9.760 | 48.887 |
| $A_{Q2}$ | 2.393 | 25.745 | 110.24 | 20.879 | 8.624 | 9.551 | 42.210 |
| $B_{Q2}$ | 0.795 | 2.379 | 20.879 | 112.85 | 1.045 | 1.133 | 74.51 |
| A | 8.734 | 2.100 | 8.624 | 1.045 | - | 0.0681 | 173.568 |
| S | 1.165 | 9.760 | 9.551 | 1.133 | 0.0681 | - | 123.543 |
| Ground | 67.797 | 48.887 | 42.210 | 74.51 | 173.568 | 123.543 | - |

**Table 3.1:** Capacitance matrix of the design obtained using electrostatic simulation Note: the diagonal elements for the qubit islands represent the total capacitance of the island with all other elements in the configuration

### 3.2.1 Estimation of Charging energy of the Qubit

The simulation of circuit in ANSYS Maxwell is done by creating a simulation vacuum cube of volume $V$. The cube length goes from $-l/2$ to $l/2$, where is $l$ coded as a variable (Fig.3.2). This way upon changing the programmed variable value, the dimensions can be changed while maintaining symmetry around origin. Then a dielectric substrate with the properties of silicon is created within the box origin (half of the box still being vacuum). A metal conductor is then added on top of the silicon substrate denoting the ground plane of the circuit. The ground plane close to origin is removed, and only the necessary metal islands are placed. The dimensions of these islands are also coded similar to vacuum box making modifications to the circuit easier. Then with voltage excitation to couplers, resonators and qubit islands a capacitance matrix is obtained.

Determining charging energy from capacitance matrix is described in [17]. The effective capacitance of an island of a qubit $C_{island}$ is sum of its capacitance to elements other than the second island of the qubit that is :

$$C_{A_{Q1}} = C_{A_{Q1}total} - C \tag{3.10}$$

with C being capacitance between the two islands and

$$C_{B_{Q1}} = C_{B_{Q1}total} - C \tag{3.11}$$

Charging energy of one qubit is given by

$$E_C = \frac{e^2}{C_\Sigma} \tag{3.12}$$

where $C_\Sigma$ is defined as

$$C_\Sigma = \frac{C_{A_{Q1}} C_{B_{Q1}}}{C_{A_{Q1}} + C_{B_{Q1}}} + C \tag{3.13}$$

For the capacitance matrix 3.1, and the transition frequency of $\omega_{ge}$ the calcu-

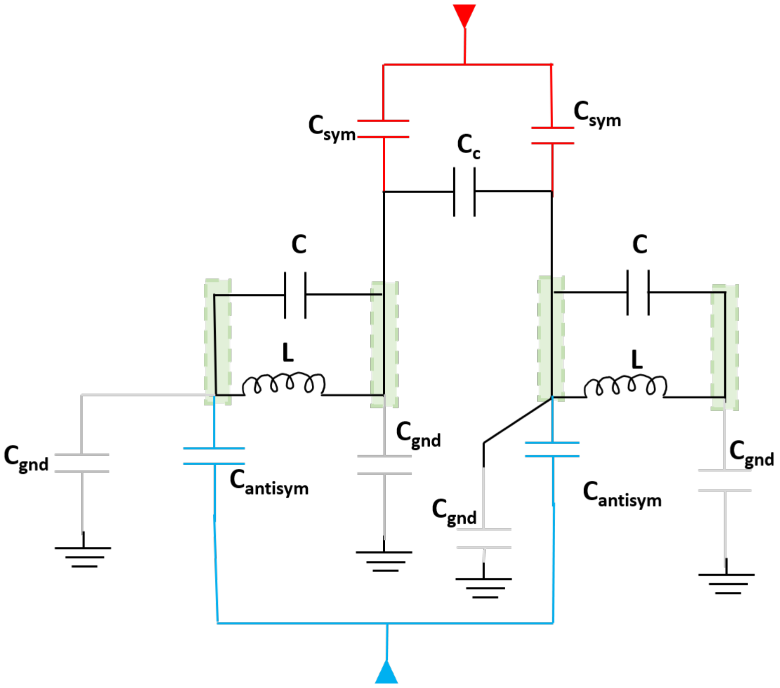

**Figure 3.3:** *Circuit equivalent of layout showing qubits as LC oscillator which are coupled to the waveguides. Islands couple to the ground through capacitance $C_g nd$. $C_c$ is the capacitance between the two qubits.*

lation is as follows

$$\begin{aligned} C_{A_{Q1}} &= 114.0 - 21.101 = 92.899 \text{ fF} \\ C_{B_{Q1}} &= 110.73 - 21.101 = 89.629 \text{ fF} \\ C_{\Sigma} &= 66.718 \text{ fF} \\ E_c/2\pi &= 289.5 \text{ MHz} \\ \text{with } \omega_{ge}/2\pi &= 6.5 \text{ GHz} \\ E_J/2\pi &= 19.87 \text{ GHz and } E_J/E_C = 68.5257 \end{aligned} \tag{3.14}$$

The two qubits are assumed to be having the same transition frequency but the Josephson junction can not be reliably fabricated having the same resistance which in turn affects the Josephson energy. This could cause the two qubits to have slightly different transition frequencies, even if their charging energies were exactly the same. For the fabrication process used in this thesis, a typical spread in resistance for nominally identical junctions fabricated on the same chip is about 1%. Based on (2.5), we thus expect the two qubit frequencies to agree within about 30 MHz. Therefore, to ensure full hybridization, the coupling strength between the two qubits should be designed to be much larger than that.

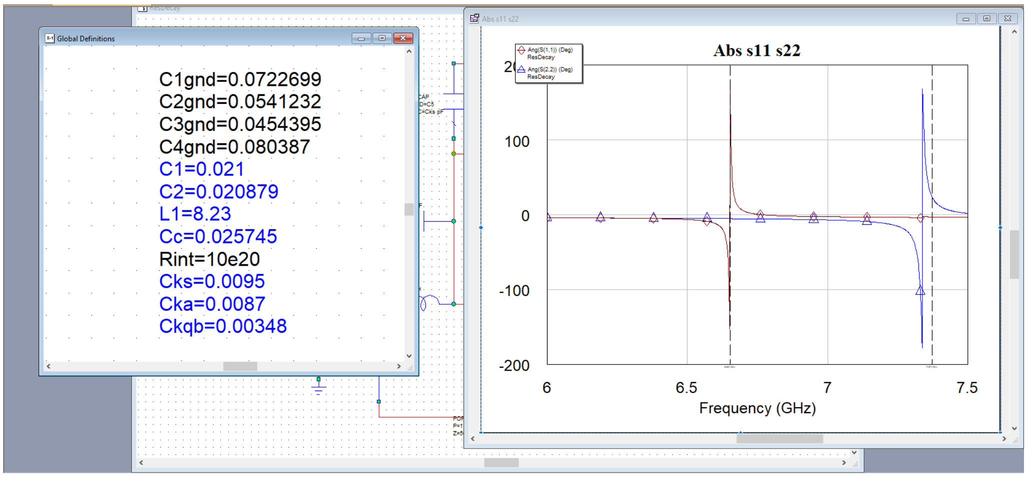

C1gnd=0.0722699
C2gnd=0.0541232
C3gnd=0.0454395
C4gnd=0.080387
C1=0.021
C2=0.020879
L1=8.23
Cc=0.025745
Rint=10e20
Cks=0.0095
Cka=0.0087
Ckqb=0.00348

**Figure 3.4:** *Snapshot of simulation of circuit showing the two modes (Red:(-) and Blue:(+)) and the capacitance values used for the simulation.*

## 3.3 Lumped element model simulation

The quantum circuit is simulated in lumped element model to determine the resonance frequency of the hybridised modes and also the coupling between the qubits. The qubits are modeled using a LC oscillator with the Capacitance between the islands ($C$) and the Josepshon junction inductance ($L$). The capacitance values for the simulation is taken from the values obtained in the electrostatic simulation. It is important to note that the capacitance is not the overall capacitance of qubit circuit ($C_\Sigma$) explained in the section above. The complete circuit is constructed as in the Fig. 3.3. The capacitive coupling between the two qubits is present and equivalent to the capacitance between the two islands.

The two waveguides are shown with the respective coupling capacitance and a port is connected to its ends to measure the response of circuit. The presence of the two modes would be seen in the phase response but not in magnitude. The response at resonance would be a $\pi$ phase shift (Fig.3.4). This circuit neglects the spurious coupling between the island and the waveguide. The Phase response does not hence show a small phase roll at the resonance frequency of the other mode. As seen by the arrangement of islands this is not true for the actual circuit. For instance the island 1 couples to the symmetric coupler and island 2 couples to the asymmetric one. We determine the coupling between the qubits to be about 250 MHz.

## 3.4 Experiment

### 3.4.1 Sample

Sample is designed in precision drawing software AutoCAD and fabricated. Two $\lambda/4$ resonators were dispersively coupled to two qubits. In notch configuration both resonators couple to a common read out waveguide. The length of 2 resonators was 6.011 mm and 6.211 mm with an estimated resonance frequency of 5.1 GHz and 4.9

| Cool down number | Sample | Wiring diagram |
|---|---|---|
| 1 | A | I |
| 2 | A | II |
| 3 | B | II |

**Table 3.2:** Different cool down conducted in this work with the sample used for measurement and its corresponding wiring diagram

GHz. The common waveguide was routed along the boundary as shown in Fig.3.5.

Initially one of the four samples was wire bonded to be measured. SGI was smaller than the minimum dimension to make a reliable wire bond (Fig.**??**). Therefore the state of symmetric grounded island in the first sample can be connected to ground, or shorted to the waveguide itself or floating (Fig. 3.5 (b)). The state of the island affects strongly the coupling between the symmetric waveguide and the symmetric mode. A second sample was prepared in which the symmetric grounded island was left floating. In both samples, the island between the arms of the anti-symmetric waveguide was successfully grounded.

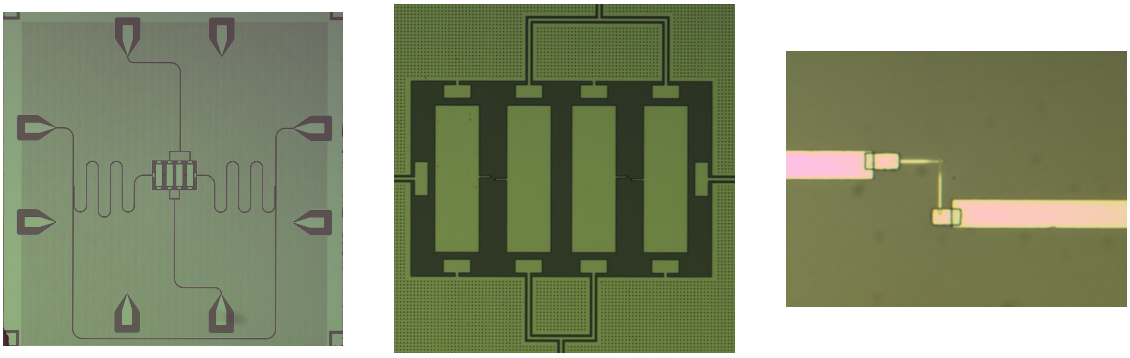

**(a)** Layout of the chip

**(b)** Zoomed in image of islands

**(c)** Josephson junction in between the islands

**Figure 3.5:** *Images of the fabricated sample. The region showing only the islands and the Josephson junction between the islands*

The sample was wire bonded to a sample holder (Fig. 3.6). Sample holder is a copper box with a mount to place the sample. The signal is carried in and out of the sample by 8 coaxial cables of which the necessary ones are connected to the lines in a cryostat. The lines from cryostat are connected to Vector Network Analyzer or signal generator which generator and acquire microwave signals from the cryostat.

### 3.4.2 Measurement setup

Both the samples used for this work was measured in a dilution crystal named 'Thor' in 3 different cool downs. The sample was measured in the mixing chamber of the cryostat at 7mK. The mixing chamber is magnetically shielded from noise sources by a mu metal and absorber. Input line of the dilution cryostat showing the attenuation of each stage.

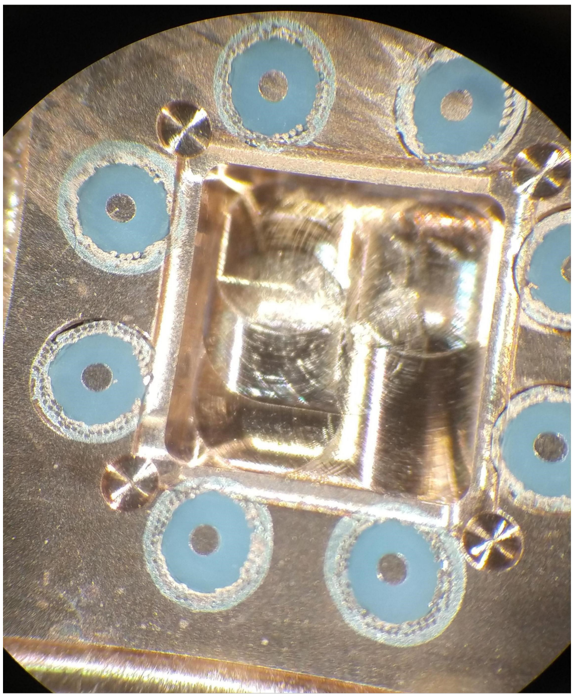

**Figure 3.6:** *Top view of the 8-port sample holder used in this thesis.*

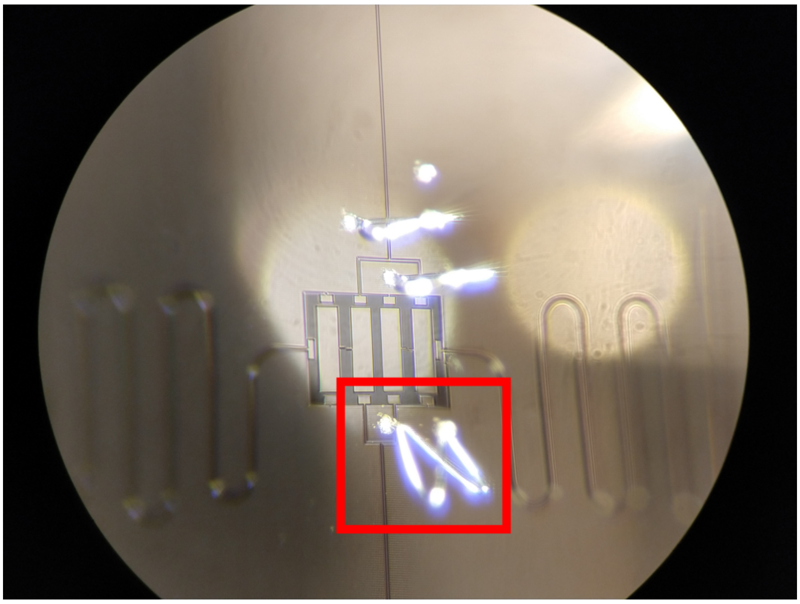

**Figure 3.7:** *Wire bonded sample. SGI is grounded to the waveguide (marked with red square).*

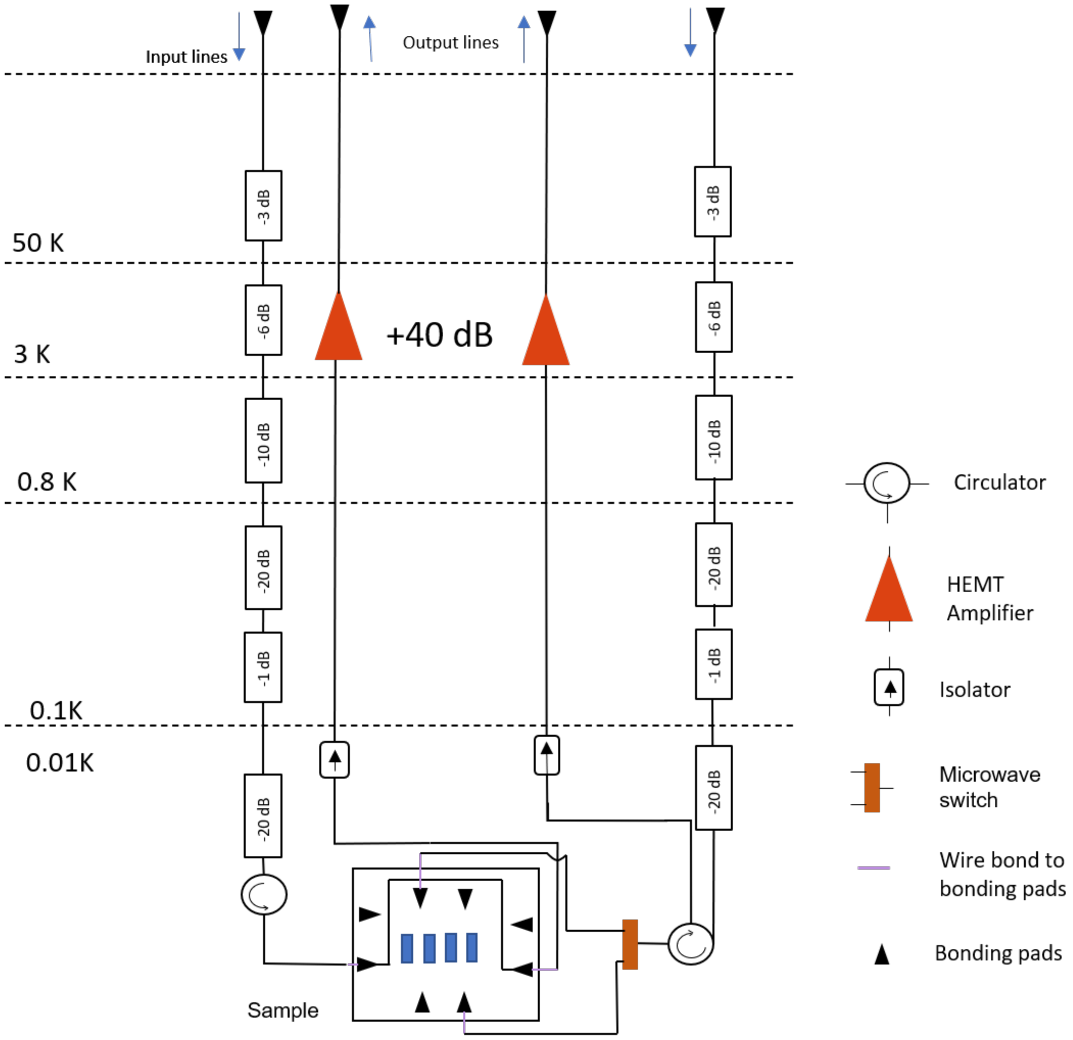

**Figure 3.8:** *Wiring diagram of the dilution cryostat showing the lines, sample, attenuation and amplification stages. A RF switch is used to multiplex read out of S and A waveguides.*

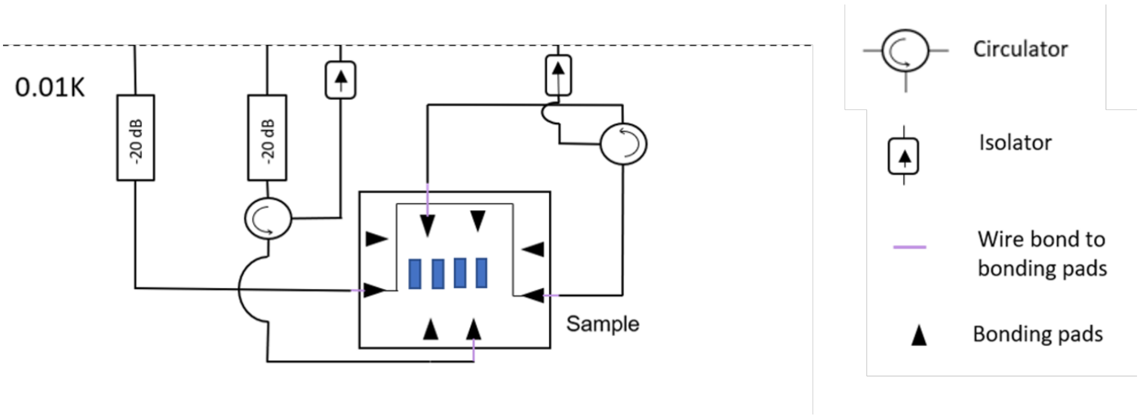

**Figure 3.9:** *Wiring diagram showing only the mixing chamber of the dilution cryostat in which a circulator is used for multiplexing read out of resonators and A waevguide*

A cryogenic circulator is used to reroute the reflected signal from the sample to the output line. The sample is placed in the indicated position. Measuring this sample presents a challenge, that is 3 elements needs to be measured with 2 lines. The first solution was multiplexing read out of waveguides by connecting it to a RF switch. The resonators have a dedicated line to be measured on. Therefore either one of the waveguide is floating when the other is being measured. In the second wiring diagram we got rid of this issue with the help of cryogenic circulator. One input-output line directly measures one waveguide. The second line measures the common waveguide coupled to resonators as well as the other waveguide. The signal is routed by input line and send to the common waveguide measuring the resonators. After the waveguide, the signal is sent to the circulator which is connected to the other waveguide. The reflected signal from the waveguide is sent to the output line through the circulator (Fig. 3.8). It is possible to route this way as the waveguides are measured in reflection and the resonators and modes have different resonance frequency. The different cool downs and wiring diagrams used in these cool downs are noted in Tab. 3.2.

Initially a broadband spectroscopy was done to determine the various modes and resonators in the sample and the first wiring diagram was used. After that reflection measurements of hybridised modes from each waveguide was done using the second wiring diagram. The results from these measurements are noted in the next chapter.

# 4

# Results

This chapter describes the results of the measurements conducted during this work. Spectroscopy of the hybridised modes are described in the first section. A discussion about the conclusions from the spectroscopy measurements and comparison of estimated and measured parameters follows the spectroscopy data.

## 4.1 Spectroscopy measurements

### 4.1.1 Hybridised modes

Initially, the response of the composite system is measured in reflection from a waveguide (either symmetric or antisymmetric) over a broad range of frequencies at a low input power. The resonators are designed for the range of 4.8 and 5 GHz which is much less than the expected range of the modes( 6 GHz ) (Fig.4.1). We expect the modes to be overcoupled to their target waveguides. The lorentzian dip of modes are identified at 5.606 GHz and 6.12 GHz (approximately). With this as resonance frequency,the reflection coefficient at different drive powers is taken. This is similar to the line cut measurement explained in Chap. 2. Using this measurement the input power range for probing the mode can be determined.

The broadband spectroscopy can give an estimate about the 3 dB bandwidth of the mode and further spectroscopy measurements will be done around the resonance frequency with four times the 3dB bandwidth estimated. This is important to get an accurate value for the decay rates in a noisy environment [23]. The spectroscopy of each mode from the target waveguide is taken with increasing power from baseline measurement till the low power limit. As shown in Fig.2.5, once the drive power is in the low power limit the mode gets saturated and the response does not change much. After the spectroscopy data is obtained a curve fitting is done to the model. The hybridised modes in the low power limit are two level systems and their behaviour for first approximation should obey the reflection from an artificial atom. So the data obtained from measurement needs to fitted to the model described by (2.6). The assumptions to fit this model are as follows

- the system is driven by a single of the waveguide
- the internal losses also includes coupling to other waveguide

The data acquisition software creates a .hdf5 file containing the measurement and the configuration used for it. The .hdf5 file can be accessed with tools like

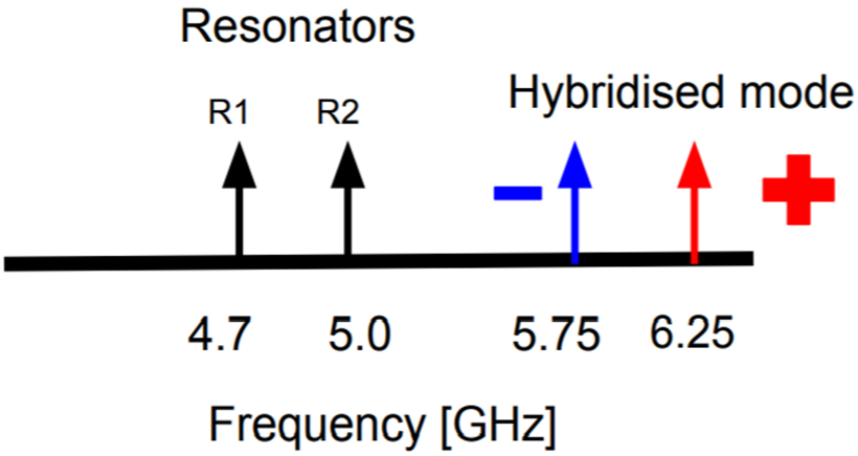

**Figure 4.1:** *The 4 different modes in the sample are shown as a function of frequency*

MATLAB or Mathematica or python language. Our data was analysed using python in Jupyter environment.Curve fitting is an optimization problem. A data set $z(x, y)$ is to be fitted to a model $\mathcal{F}(A, B, C, D, x, y)$ such that $(A, B, C, D)$ minimizes the residue of $\mathcal{F}$ and $z$. The residue (for $i^{th}$ data point) and overall cost function is calculated as follows

$$\begin{aligned} res &= \mathcal{F}(A, B, C, D, x_i, y_i) - z(x_i, y_i) \\ cost &= \sum_{i=1}^{N} |res|^2 \end{aligned} \tag{4.1}$$

The parameters $(A, B, C, D)$ minimizes the *cost* function. In Python optimization and curve fitting routines are a part of the scipy.optimize library. The usage of function curve_fit for standard curve fitting is well documented. But since the function expects only floating point data and fitting magnitude alone is insufficient for our analysis, we cannot use curve_fit. The optimization has a least mean fit routine *least_square* with which the data was fit.

The highest power $(\Omega_p »\Gamma/\sqrt{2})$ response of the composite system acts the baseline measurement and measurement at lower powers is normalized to this power. Since the baseline measurement is also normalised, in IQ plane all points of this measurement are one on the real axis. After normalization, the data of low power trace in IQ plane will be a circle. The off resonant point, $f \to \pm\infty$ will also lie on (1.0,0) in the IQ plane. If the mode is overcoupled, the trace at low power will have its resonant point on the real axis but with a $\pi$ phase change. The measurement after normalization can produce a distorted circle on the IQ plane. This can be modelled by an environment [23] which is characterized by an electrical delay $\tau$ and factor $ae^{i\alpha}$. There is delay because the measuring cable have finite length and having finite speed light takes time to reach the VNA. In curve fitting these distortions can be accounted for either by a phase the equation as in [23] or can be phase corrected

| | $\omega/2\pi$ [GHz] | $\Gamma/ 2\ \pi$ [MHz] | $\Gamma_{nr}\ /\ 2\ \pi$ [MHz] | L [dB] |
|---|---|---|---|---|
| Antisymmetric mode (-) | 5.6063 | 1.1594 | 0.4657 | 109.495 |
| Symmetric mode (+) | 6.1227 | 6.9544 | 0.0135 | 117.223 |

**Table 4.1:** Decay rates and line attenuation(L) measured in the experiment

after normalizing with baseline measurement. The process correcting the phase is discussed in Appendix A.

The 4 parameters in the Eqn.(2.6) needs to be determined by the fitting procedure. At low power, the response is independent of the drive power so the lorentzian can be fitted to the equation

$$S_{11} = 1 - \frac{2\Gamma(\Gamma + \Gamma_{nr} + 2i\Delta)}{\Gamma^2 + \Gamma\Gamma_{nr} + \Gamma_{nr}^2 + 4\Delta^2} \tag{4.2}$$

As result of fitting this equation we get the coupling rate $\Gamma$, non radiative decay rate $\Gamma_{nr}$, and the resonance frequency $\omega_{ge}$. The attenuation of the line will be determined by fitting reflection traces at different drive power. The advantage of non linear system is that, it is possible to determine the attenuation of the line as its response changes with power. Line attenuation is necessary to be known if thermal photons needs to be sent in the line.

The global fit of traces at different drive power is obtained by calculating a modified cost function which sums the residues over all the power traces. The results from the fits are discussed below.

### 4.1.2 Antisymmetric mode

After the Antisymmetric mode is identified at 5.606 GHz, a low power spectroscopy of the mode is taken at -52 dBm. The plot of this measurement in magnitude, phase, and IQ plane is shown in Fig.4.2. This results in the parameters, $\Gamma/2\pi$ as 1.15 MHz, $\Gamma_{nr}/2\pi$ as 0.4016 MHz and $\omega_{mode}$ as 5.60628 GHz.

These values can be used as initial values to determine the attenuation of the line by fitting the reflection spectroscopy data at different drive powers. As shown in Fig. 4.3 the data is in good agreement with the model. Line attenuation obtained from fits is -109.495 dB which is a good estimation as -40 dB attenuation was used at the output of VNA and -69.5 dB is the attenuation from the drive line.

### 4.1.3 Symmetric mode

The Symmetric mode (+) is a higher energy mode found at 6.12 GHz for the first sample. A low power spectroscopy is taken at -24 dBm. A least square fit of this data to the model (4.2) would result in $\Gamma/2\pi$ as 6.952 MHz, $\Gamma_{nr}/2\pi$ as 0.0135 MHz and resonance frequency as 6.1227 GHz. The coupling between the symmetric mode and symmetric waveguide is about six times larger than the coupling between antisymmetric mode and antisymmetric waveguide. Then spectroscopy at different powers in the power range 5 dBm to -24 dBm is taken. These measurement are normalised to baseline measurement and compensated for electrical delay. Then

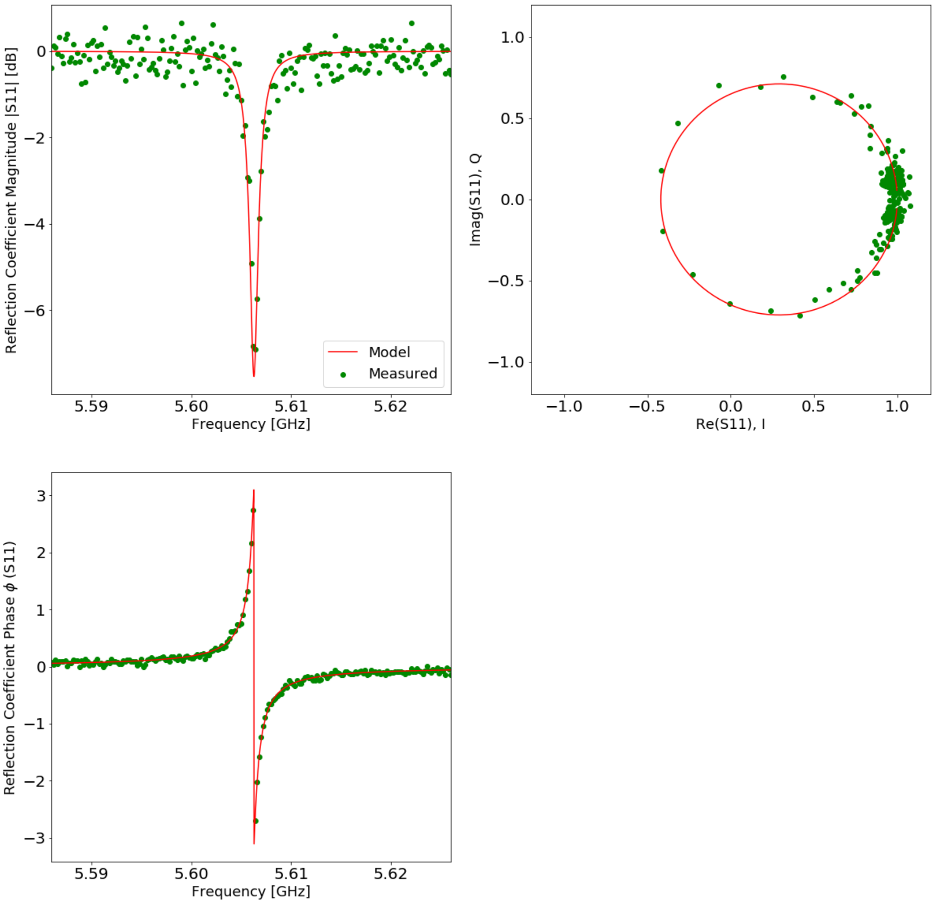

**Figure 4.2:** *The reflection measurement of the Antisymmetric mode (-) from the Antisymmetric waveguide (A) at -52 dBm drive power in magnitude, phase and IQ plane.*

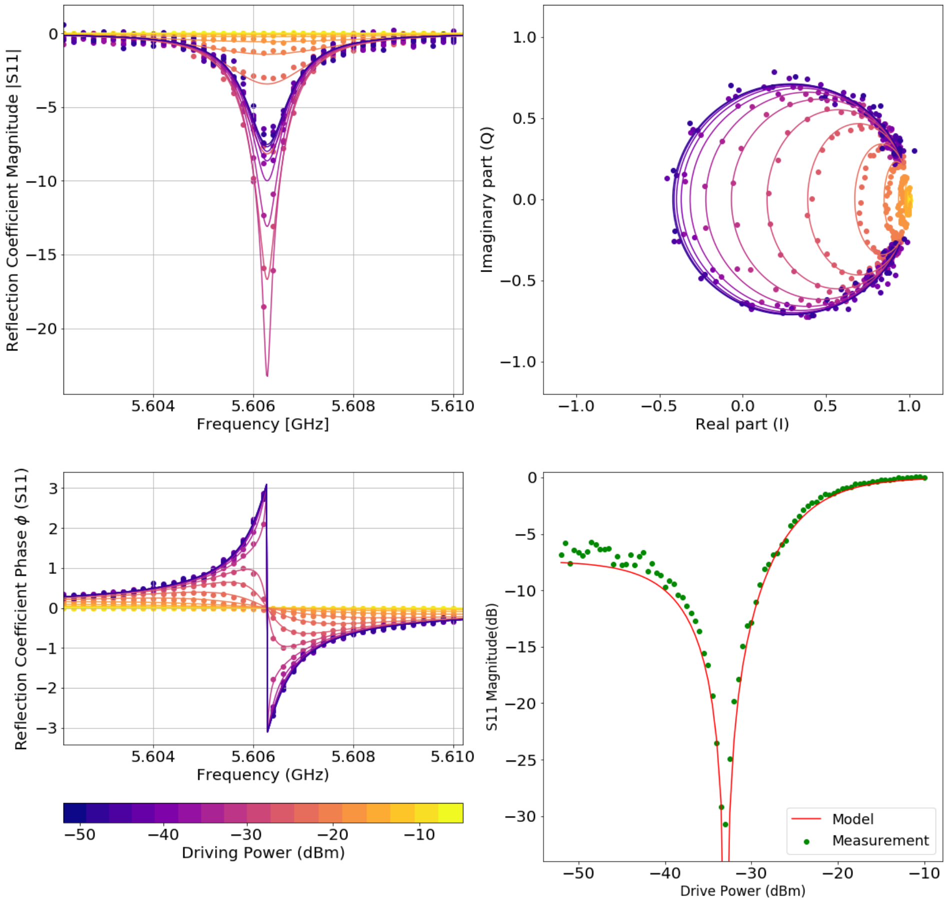

**Figure 4.3:** *Spectroscopy measurement of Antisymmetric mode from Antisymmetric waveguide of the first sample.*

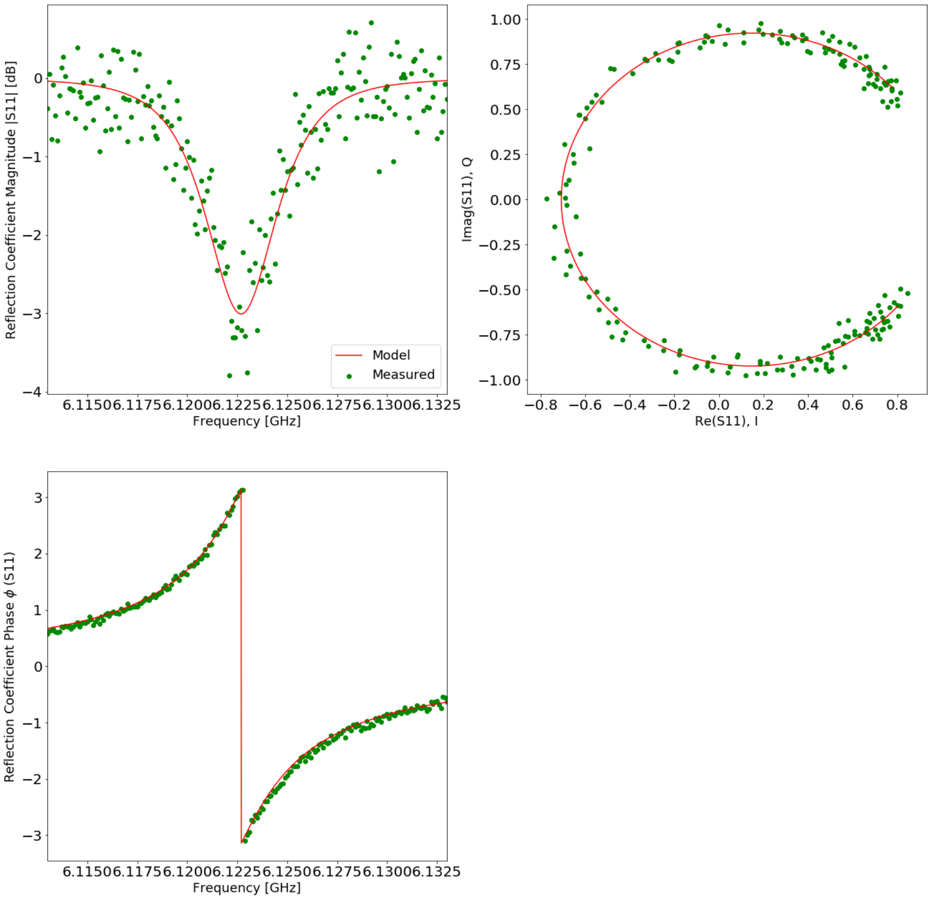

**Figure 4.4:** Spectroscopy measurement of symmetric mode from symmetric waveguide at -24 dBm

data is fitted to the full model in Eqn.(2.6). The data and the fitted model are shown in the Fig.4.5. There is good agreement between the data and the model. The line cut at resonance for different power traces also follow the same trend as shown in Fig.4.5. Decay rates and line attenuation parameters of the two modes are noted in 4.1.

### 4.1.4 Broadband spectroscopy measurement

Broadband spectroscopy taken with both the Antisymmetric (A) and Symmetric (S) waveguides connected to the same switch.Since one of the waveguides is left floating, both modes (+ and -) are overcoupled to the measuring waveguide. A spectroscopy taken from antisymmetric waveguide in such a setup is shown in Fig. 3.9 .

Fig. 4.6 shows a spectroscopy of span 700 MHz (5.5 GHz to 6.2 GHz). Three

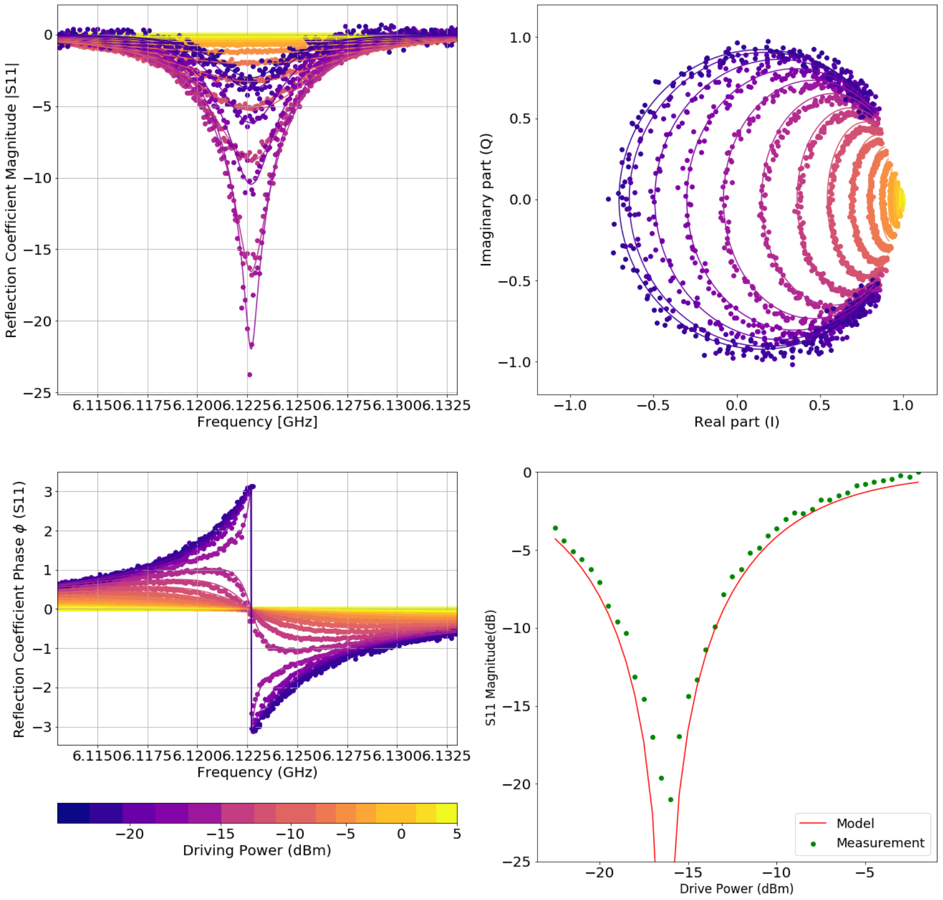

**Figure 4.5:** Spectroscopy of symmetric mode from the symmetric waveguide at different drive power

different modes are visible. Antisymmetric mode is measured by the lorentzian at 5.606 GHz, the Symmetric mode at 6.12 GHz. and a second order transition at 6.04 GHz. The second transition is used to calculate the anharmonicity of the qubits using the equation

$$\omega_{sc} = \omega_{ge} + 1/2(\alpha + \sqrt{16g^2 + \alpha^2}) \tag{4.3}$$

with $\omega_{ge}$= 5.875 GHz, we get $\alpha$ as 377 MHz.

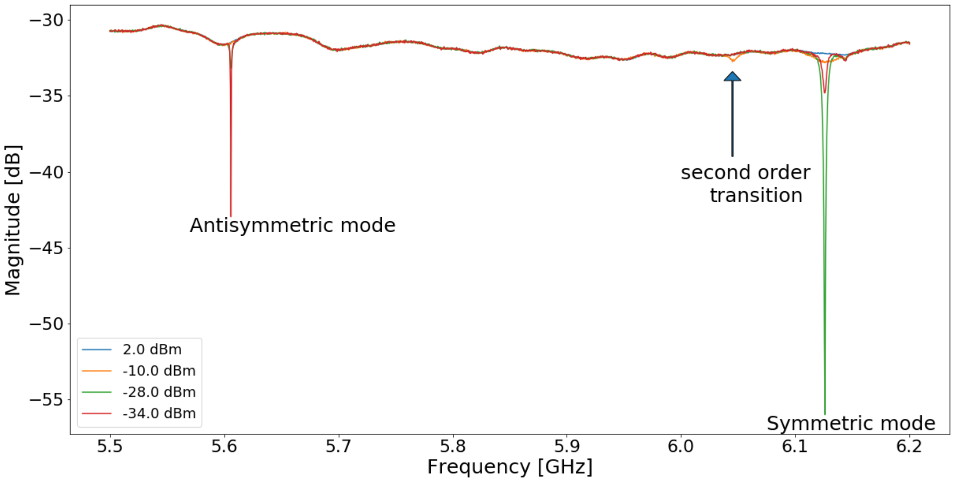

**Figure 4.6:** Broadband spectroscopy from Antisymmetric waveguide (A) showing Antisymmetric mode, Symmetric mode and a second order transition.

## 4.2 Discussion

A comparision between the obtained values of the sample and the estimated values from design are shown in Tab. 4.2. Circuit parameters can be calculated from the results described above. The transition frequency of the qubits can be calculated by $\frac{(\omega_{antisym}+\omega_{sym})}{2}$. As described in Chapter. 2 the coupling between qubits can be calculated by $\frac{(\omega_{sym}-\omega_{antisym})}{2}$. The second order transition can be used to calculate the anharmonicity of the qubit (using Eqn. 2.11) and it is determined to be 377 MHz. The mismatch in the Josepshon junction could result in different transition frequency for the qubits or lead to detuning of the qubits.

The spectroscopy measurements show that coherent scattering from the hybridised mode follows the model of coherent scattering by a two level system. The decay rate of symmetric mode (+) to symmetric waveguide (S) is higher than that of antisymmetric mode (-) to anisymmetric waveguide (A). This is not a feature of the design since the dimensions of coupler and capacitance between the islands and the waveguides are the same. The symmetric grounded island is probably shorted to the waveguide which resulted in about six times higher coupling of the symmetric mode than antisymmetric mode to its target waveguide. This can also explain the higher $\Gamma/\Gamma_{nr}$ of the symmetric mode than the antisymmetric mode in the first

| Parameter | Design | Measured |
|---|---|---|
| Qubit frequency | 6.5 GHz | 5.875 GHz |
| Coupling between qubits | 250 MHz | 275 MHz |
| Charging energy | 300 MHz | 377 MHz |
| $\omega_{res1}$ | 4.9 GHz | 4.5 GHz |
| $\omega_{res2}$ | 5.1 GHz | 4.76 GHz |

**Table 4.2:** Comparison of circuit parameters estimated for the design and obtained from analysis of measurement data of the sample

sample. The dependence of decay rates can be calculated by black box quantizing the circuit shown in Fig.3.3.

# 5

# Conclusion

In this work the decay rates of hybridised modes into coupled waveguides was studied. A sample with two capacitively coupled split transmon qubits was designed and fabricated. The spectroscopy measurements revealed that the transitions from hybridised mode behave the same way as a two level system transitions. It was also found the decay rate of symmetric mode to its target waveguide is much larger than decay rate of antisymmetric mode to its waveguide. Also the ratio of coherent scattering to incoherent scattering, $\Gamma/\Gamma_{nr}$ is larger for the symmetric mode.

Quantum measurement cooling experiments would require this feature and therefore increasing coupling between the island and the waveguide couplers would result in a better sample to conduct the experiment. Increasing the length of the qubit islands would decrease the direct coupling between the waveguides decreasing the non radiative decay. This would lead to a decrease in anharmonicity. By the exponential dependence of noise dispersion of a transmon qubit the non radiative decay channels of modes might further reduce. Waveguide couplers can be enclosed by the islands which would lead to further shielding of the coupler and increase the coupling between island and waveguide.

The theoretical understanding of affect of radiative and non radiative decay rates should be investigated. If significant decay rates are obtained then the quantum measurement cooling experiment should be conducted leading to understanding of role of quantum coherences in heat transport.

# Bibliography

[1] L. Buffoni, A. Solfanelli, P. Verrucchi, A. Cuccoli, and M. Campisi, "Quantum Measurement Cooling", Phys. Rev. Lett. 122, 070603

[2] O. Astafiev, A. M. Zagoskin, A. A. Abdumalikov, Yu. A. Pashkin, T. Yamamoto, K. Inomata, Y. Nakamura, and J. S. Tsai, "Resonance Fluorescence of a Single Artificial Atom" Science 12 Feb 2010: Vol. 327, Issue 5967, pp. 840-843 DOI: 10.1126/science.1181918

[3] C. G. Knott. "Quote from undated letter from Maxwell to Tait". Life and Scientific Work of Peter Guthrie Tait. Cambridge University Press. pp. 213–215, 1911.

[4] L. Szilard, "Über die Entropieverminderung in einem thermodynamischen System bei Eingriffen intelligenter Wesen (On the reduction of entropy in a thermodynamic system by the intervention of intelligent beings)". Zeitschrift für Physik. 53 (11–12): 840–856, 1929.

[5] R. Landauer, "Irreversibility and heat generation in the computing process". IBM Journal of Research and Development. 5 (3): 183–191. doi:10.1147/rd.53.0183. Retrieved November 13, 2014. reprinted in Vol. 44, No. 1, January 2000, p. 261, 1961.

[6] J. Preskill, "Quantum Computing in the NISQ era and beyond", Verein zur Förderung des Open Access Publizierens in den Quantenwissenschaften, Vol 2, 79, 2018.

[7] A. Bérut, A. Petrosyan and S. Ciliberto, "Information and thermodynamics: experimental verification of Landauer's Erasure principle", IOP Publishing, Published 10 June 2015.

[8] J. V. Koski, V. F. Maisi, J. P. Pekola, and D. V. Averin, "Experimental realization of a Szilard engine with a single electron", PNAS September 23, 2014 111 (38) 13786-13789.

[9] M. Campisi, J. Pekola , and R. Fazio, "Non equilibrium fluctuations in quantum heat engines: theory, example, and possible solid state experiments". New J. Phys. 17 (2015), 035012.

[10] F. Arute et al., “Quantum supremacy using a programmable superconducting processor,” Nature, vol. 574, pp. 505–510, 2019.

[11] N. Cottet, S. Jezouin, L. Bretheau, P. Campagne-Ibarcq, Q. Ficheux, J. Anders, A. Auffèves, R. Azouit, P. Rouchon, and B. Huard "Observing a quantum Maxwell demon at work," Proceedings of the National Academy of Sciences, vol. 114, no. 29, pp. 7561–7564, 2017.

[12] A. Ronzani,, B. Karimi, J. Senior, Y.C. Chang, J. T. Peltonen, C.D. Chen and Jukka P. Pekola "Tunable photonic heat transport in a quantum heat valve," Nature Physics, vol. 14, p. 991, 2018.

[13] M. Naghiloo, J. J. Alonso, A. Romito, E. Lutz, and K. W. Murch, "Information Gain and Loss for a Quantum Maxwell's Demon," Phys. Rev. Lett., vol. 121, no. 3, p. 30604, Jul. 2018.

[14] A. Blais , S.M. Girvin, and W.D. Oliver, "Quantum information processing and quantum optics with circuit quantum electrodynamics" . Nat. Phys. 16, 247–256 (2020).

[15] J. P. Martínez, S. Léger, N. Gheeraert, R. Dassonneville, L. Planat, F. Foroughi, Y. Krupko, O. Buisson, C. Naud, W. H. Guichard, S. Florens, I. Snyman and N. Roch, "A tunable Josephson platform to explore many-body quantum optics in circuit-QED". npj Quantum Inf 5, 19 (2019). https://doi.org/10.1038/s41534-018-0104-0

[16] J. Koch, T.M. Yu, J. Gambetta, A. A. Houck, D. I. Schuster, J. Majer, A. Blais, M. H. Devoret, S. M. Girvin and R. J. Schoelkopf, "Charge-insensitive qubit design derived from the Cooper pair box", Phys. Rev. A 76 042319 (2007).

[17] M.Pechal, "Microwave photonics in superconducting circuits", [Doctoral dissertation, ETH ZURICH] (2016).

[18] M. Göppl, A. Fragner, M. Baur, R. Bianchetti, S. Filipp, J. M. Fink, P. J. Leek, G. Puebla, L. Steffen, and A. Wallraff, "Coplanar waveguide resonators for circuit quantum electrodynamics", Journal of Applied Physics 104, 113904 (2008)

[19] A.F. Kockum, "Quantum optics with artificial atoms", [Doctoral dissertation, Chalmers University of Technology] (2014).

[20] Y. Nakamura, Yu. A. Pashkin and J. S. Tsai, "Coherent control of macroscopic quantum states in a single-Cooper-pair box", Nature 398, 786-788 (1999), doi:10.1038/19718, arXiv:9904003.

[21] D. Vion, in Quantum entanglement and information processing (Les Houches Session LXXIX), edited by J.-M. Raimond, J. Dalibard, and D. Esteve (Elsevier, 2003), pp. 443–485.

[22] M. Scigliuzzo, A. Bengtsson, J. C. Besse, A. Wallraff, P. Delsing, and S. Gasparinetti, "Primary thermometry of propagating microwaves in the quantum regime", (2020), arXiv:2003.13522 [quant-ph].

[23] S. Probst, F. B. Song, P. A. Bushev, A. V. Ustinov, and M. Weides, "Efficient and robust analysis of complex scattering data under noise in microwave resonators", Rev. Sci. Instrum. 86, 024706 (2015).

[24] S. Wuensch, G. Hammer, T. Kappler, F. Geupert, and M. Siegel, "Investigation and Optimization of LEKID Coupling Structures and Multi-Pixel Arrays at 4.2 K", IEEE Transactions on Appl. Superconductivity 21, 752 (2011).

[25] Y. Chen, D. Sank, P. O'Malley, T. White, R. Barends, B. Chiaro, J. Kelly, E. Lucero, M. Mariantoni, A. Megrant, C. Neill, A. Vainsencher, J. Wenner, Y. Yin, A. N. Cleland, and J. M. Martinis, "Planar superconducting resonators with internal quality factors above one million", Applied Physics Letters 101, 182601 (2012).

[26] M. R. Vissers, M. P. Weides, J. S. Kline, M. Sandberg, and D. P. Pappas, "Identifying capacitive and inductive loss in lumped element superconducting hybrid titanium nitride/aluminum resonators", Applied Physics Letters 101, 022601 (2012).

# A

# Second sample characterization

In order to understand the state of the SGI (**mention before**) we measured the the second sample. The measurement would also verify the parameters like qubit frequency, coupling rate and decay rates ofeach mode of our design. It is worthy noting that the size of the island does not change and the wire bonding is still a challenge. One can be sure of wire bonding only if the island is left floating. These measurement can not conclude if the decay rates of modes to their target waveguide is equal for symmetric and antisymmetric mode because this island is left floating. This sample was measured using the wiring diagram shown in Fig. 3.9 using the cryogenic circulator.

**Antisymmetric mode**

The spectroscopy of the (-) mode was measured with 21 different input power. The baseline measurement was at 0 dBm. Data analysis was done similar to the first sample in which the low power traces were fit to a model without power dependence. The parameters resulting in a better fit was used as guess values to perform a global fit in which the traces at different drive powers were fit. The decay rates obtained from such a fitting are tabulated in Fig.A.1. Antisymmetric mode of the second sample is found at 5.630 GHz. The coupling between - and A is found to be about 1.43 MHz with a non radiative decay of 0.1774 MHz which are comparable to decay rates measured in the first sample.

**Symmetric mode**

The (+) mode spectroscopy measurement was taken with a baseline drive power of 0 dBm and with 20 different drive powers below 0 dBm. After normalization the measurement data is as shown in A.2. These graphs show that the baseline measurement was at lower power (with $\Omega_p < 16\Gamma$) than the actual baseline power which is indicated by some of the traces at high power having a magnitude greater than 1 which is not possible according to the model presented in 2.5. Also due to this in the IQ plane, the measurement crosses the point (-1.0,0.0). The spectroscopy was not further analyzed. But measurement in which line cut at resonance was measured was analyzed to find the parameters noted in the Table.A.1. According to these parameters the + mode decay rate to S is dependent on the grounding of SGI. Since in the first sample, SGI was shorted to the S waveguide the coupling was highest and when SGI was left floating coupling is still higher than estimated by design. Line attenuation for these measurement is different from the measurement of - mode from A waveguide as room temperature attenuation was changed before it.

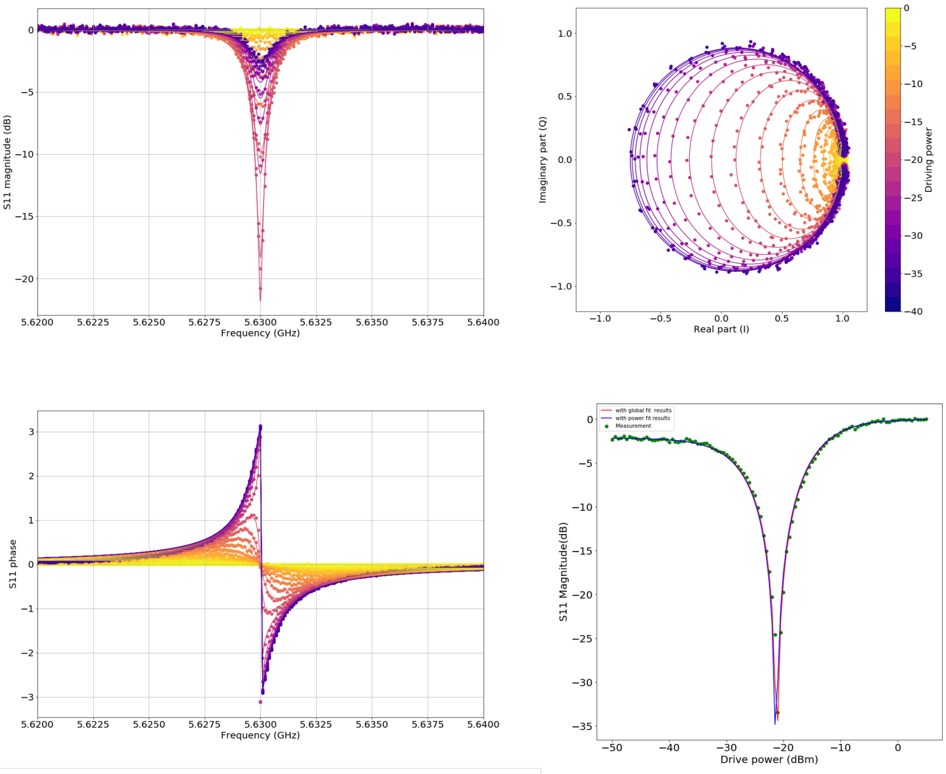

**Figure A.1:** *Spectroscopy measurement and overlaid fitted model of (-) from A of the second sample*

| | $\omega/2\pi$ [GHz] | $\Gamma/$ 2 $\pi$ [MHz] | $\Gamma_{nr}$ / 2 $\pi$ [MHz] | L [dB] |
|---|---|---|---|---|
| Antisymmetric mode (-) | 5.630 | 1.43 | 0.18 | 119.616 |
| Symmetric mode (+) | 6.136 | 2.26 | 0.12 | 98.452 |

**Table A.1:** The Decay rates and line attenuation measured using spectroscopy of the two modes of second sample

## A.1 Characterization of Resonators

As described in the design, measurement based dephasing is achieved by measuring qubits in their eigen basis. In the design of this thesis dispersively coupled $\lambda/4$ resonators measure the qubits in their eigen basis. The resonators are coupled to a transmission for multiplexed read out in the notch configuration. The $\lambda/4$ resonators were read out in reflection. The reflection from a resonator is power independent, as adding photons (of same frequency) increases the quantum state on the resonator. The quality factors of resonator can be determined by fitting the reflection to a complex lorentzian A.1. The resonance frequency and quality factors obtained from circle fit are tabulated in Table.A.2.

$$S_{21}^{notch} = ae^{i\alpha}e^{-i2\pi}\left[1 - \frac{(Q_l/|Q_c|)e^{i\phi}}{1 + 2iQ_l(f/f_r - 1)}\right] \tag{A.1}$$

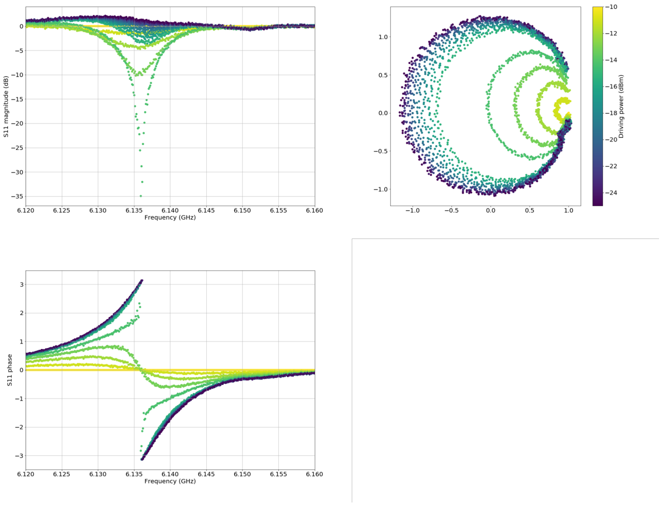

**Figure A.2:** *Spectroscopy measurement of (+) mode from S of the second sample*

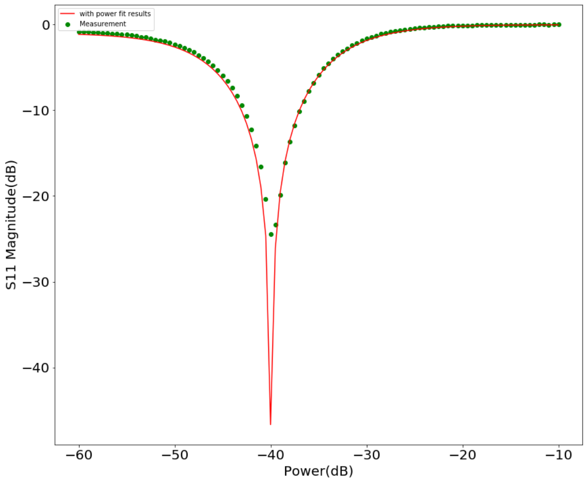

**Figure A.3:** *Resonant measurement of the + mode from the S symmetric waveguide of the second sample*

| Properties | Sample 1 | | Sample 2 | |
|---|---|---|---|---|
| Resonance frequency | 4.725 GHz | 4.581 GHz | 4.726 GHz | 4.584 GHz |
| Internal quality factor | 38901.78 | 362026.62 | 783959.44 | 186262.86 |
| Coupling quality factor | 19218.66 | 16070.30 | 41992.060 | 38299.57 |
| Loaded quality factor | 12880.11 | 15810.87 | 44387.79 | 31817.58 |

**Table A.2:** Resonance frequency and Quality factors of the resonators obtained from performing circle fit on reflection measurements

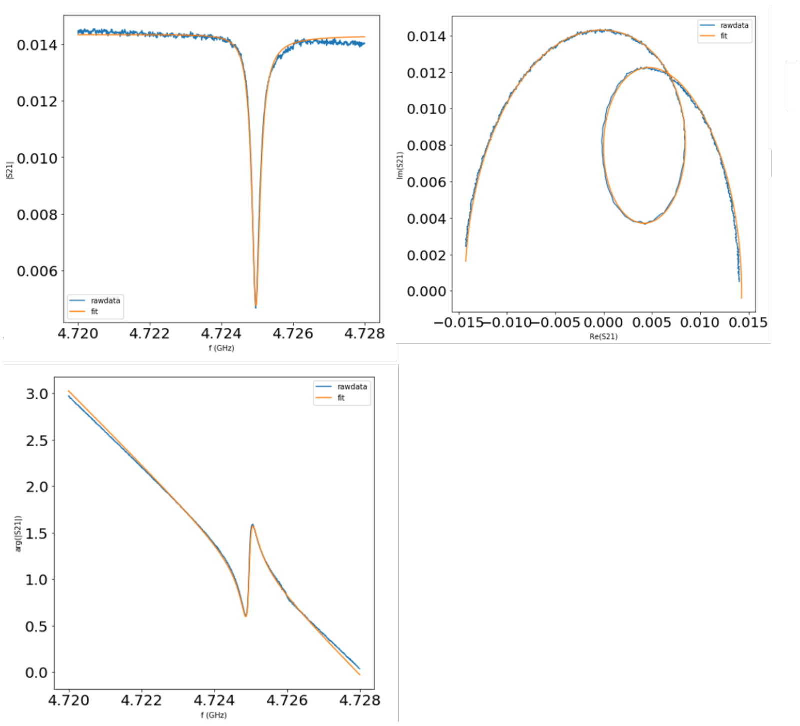

**Figure A.4:** *Reflection measurement and its fit on the resonator measured in the first sample*

The measurement from resonators is fit using Circle fit method described in [23]. Measurement with their fits are shown in Fig.A.4. The coupling between the qubit and resonator results in shift of its resonance frequency. If only qubit and a resonator are coupled this shift can be determined by $2g^2/\Delta$. But of the composite system the dispersive shift is different and theoretical calculations would determine the exact dispersive shift.

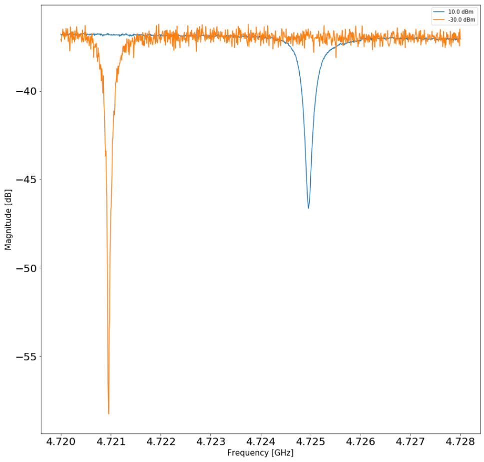

**Figure A.5:** *Dispersive shifts of resonator coupled to qubits*

# B

# Electrical delay calculation

When microwave signal travels through a finite length cable it undergoes phase change. These rotations of phase persists as the attenuation and amplification stages only modify the amplitude of the signal. Spectroscopy data shown in Fig.B.1(a) is expected to be circles at the low power but it is distorted. Also the response at different powers does not follow the same pattern due to these distortions. In the phase plane the

Electrical delay phase change can be noticed in data in the IQ plane and phase response of the signal. The reflection measurement (spectroscopy) of the hybridised mode to its target waveguide suffered such a phase change. The phase change can be modified by product of signal with a complex phase factor. Firstly, it is determined if the phase change is present in response for all frequencies by equal amount (which is an offset to the phase response) then the average of the offset (phase) is calculated for initial frequencies Fig.B.1(). If the phase change has a gradual change Figure.B.1(b) then the phase is determined by the average of phase ($\varphi$) at the phase of initial frequency response and final frequency response. The complex phase $e^{-j\varphi}$ is multiplied to the actual response.

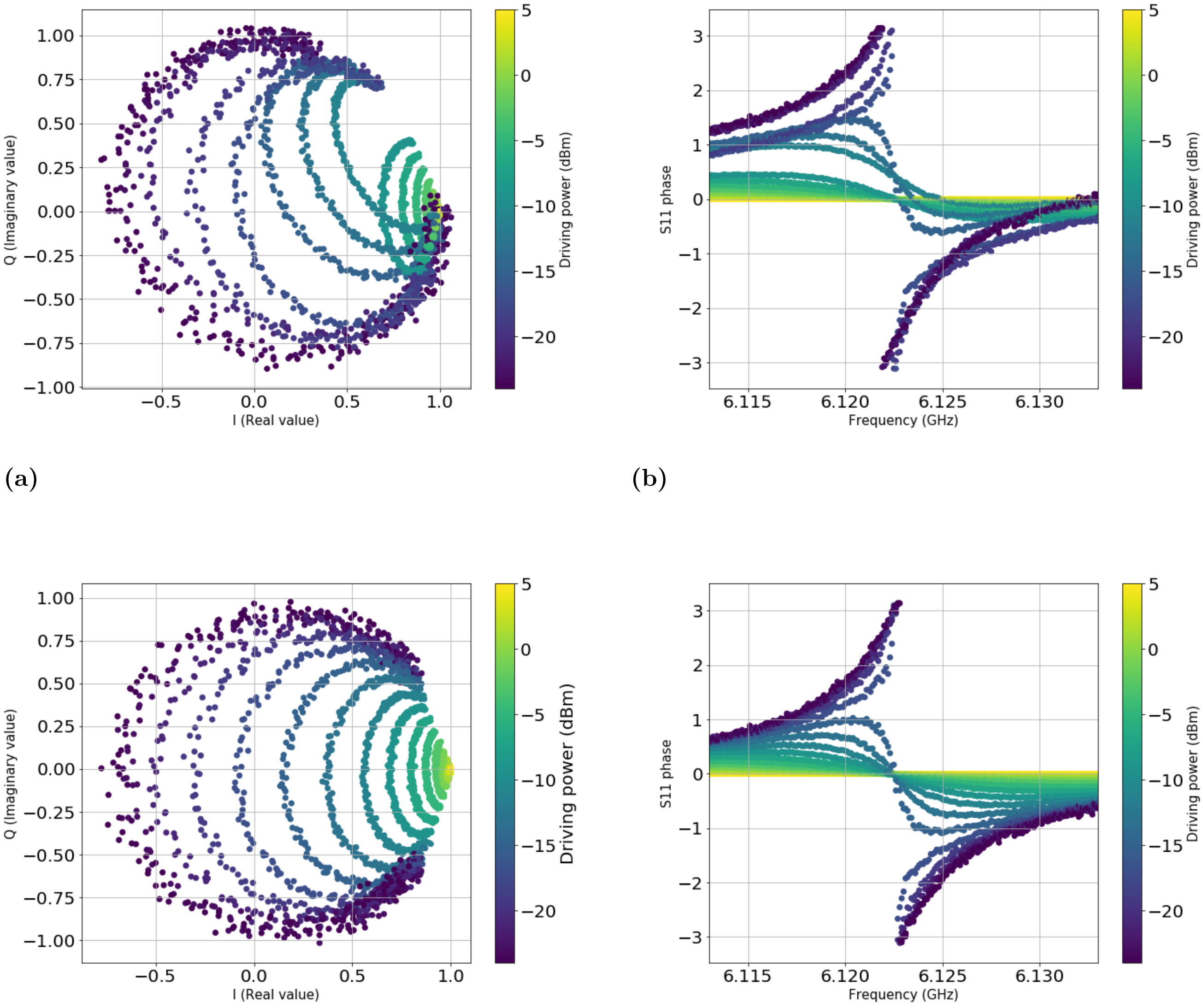

**(a)** **(b)**

**(c)** **(d)**

**Figure B.1:** *Reflection spectroscopy of the symmetric mode (+) from the symmetric waveguide (S) before and after electrical delay phase correction. (a), (b) is respectively the IQ plane and the phase response of the raw signal while the (c), (d) is respectively the IQ plane and the phase response of the phase delay corrected signal.*

# C

# Scripts used for data analysis

This section contains the python scripts used to ou

```
#Load the libraries
import numpy as np #math library
import matplotlib.pyplot as plt #plot library
import sys
sys.path.append("C:\Program Files\Labber\Script")
import Labber #Labber library for data handling
from scipy import optimize #fit function
from matplotlib import cm
cmap = cm.get_cmap(’plasma’,16)
from matplotlib import colors as col
plt.rc(’xtick’, labelsize=20)
plt.rc(’ytick’, labelsize=20)


#import data file
PATH=r’C:\Users\exp\2020_02_01\antisymmetric_diff_powers.hdf5’

#read measurement
file=Labber.LogFile(PATH)
print(’Imported data from: ’, PATH)

#read sweeps
step_channels = file.getStepChannels()
print(’\nThere are’, len(step_channels),’step channels:’ )

for i in range(len(step_channels)):
#read the frequencies recorded in the spectroscopy
    if step_channels[i][’name’]=="4ports VNA - Center frequency":
        f0cf=step_channels[i][’values’]
    if step_channels[i][’name’]=="4ports VNA - Span":
        f1s=step_channels[i][’values’]
#number of points in each trace
    if step_channels[i][’name’]=="4ports VNA - # of points":
        pointN=step_channels[i][’values’]
#different drive powers at which the trace is taken
    if step_channels[i][’name’]=="4ports VNA - Output power":
        powers=step_channels[i][’values’]

#calculating frequency range using center frequency and span
f0 = f0cf-f1s/2
f1 = f0cf+f1s/2

frequencies=np.linspace(f0, f1, int(pointN))
```

```
#multiple traces of frequency points for better data representation
newFreq=np.zeros((len(powers),len(frequencies)))
for i in range(len(powers)):
    for j in range(len(frequencies)):
        newFreq[i,j]=frequencies[j]

# function to obtain reflection traces
S11 = np.zeros((len(powers),len(frequencies)))+1j*np.zeros((len(powers),len(frequencies)))
for i in range(file.getNumberOfEntries()):
        S11[i] = getAtrace(file,i,’4ports VNA - S21’)

S11_new=np.zeros((len(powers),len(frequencies)))+1j*np.zeros((len(powers),len(frequencies)))

#Renormalize the reflection to a high power trace
for i in range(len(frequencies)):
    for j in range(len(powers)):
            S11_new[j,i]=S11[j][i]/S11[0][i]

S11=np.conj(S11_new)

ph=np.linspace(0.0, 1.0, num=len(powers))

for i in range(len(powers)):
    trace =S11[i]
    ph_sum=0.0
    for j in range(10):
        ph1=np.angle(trace[j])
        ph2=np.angle(trace[(len(frequencies)-(j+1))])
        ph_sum+=(ph1+ph2)/2
    ph[i] = ph_sum/10.0
    S11_new[i] = np.exp(-1j*ph[i])*S11[i]
S11=S11_new


#*******************************************************************
#defining function to fit the low power trace and its corresponding cost function
#*******************************************************************

def lor(f,gamma,gammanr,f0):
    return (1 - (2*gamma*(gamma+gammanr+2*1j*2*np.pi*(f-f0)))/(gamma**2+2*gamma*gammanr+gammanr**2+4*(2*np.pi*(f-f0))**2))

def cost(x, f, data):
    totalCost=0
    for i in range(len(f)):
            res=lor(f[i],x[0],x[1],x[2])-data[i]
            totalCost+=(np.abs(res))**2
    return totalCost

last_pow=S11[powers[len(powers)-1]]

x0 =np.array([7.0e6,2.8e6,5.606e9])

```

```python
initialCost=cost(x0,frequencies,last_pow)
print('Initial cost = ', initialCost)
res = optimize.least_squares(cost,x0,bounds=([3.0e6,0.1e6,5.6e9],[8.0e6,4.0e6,5.61e9]),verbose=2,args = (frequencies,last_pow))
print('final cost=',cost(res.x,frequencies,last_pow))
print(res.x)
print('gamma is:',res.x[0]/(2*np.pi*1e6),'(MHz), gammanr is:',res.x[1]/(2*np.pi*1e6),'(MHz), mode frequency:',res.x[2]/1e9)



#*********************************************************
#defining functions to fit traces at different powers
#*********************************************************

def lor1(f,power,gamma,gammanr,f0, A):
    return (1 - (2*gamma*(gamma+gammanr+2*1j*2*np.pi*(f-f0)))/(gamma**2+2*gamma*gammanr+gammanr**2+4*(2*np.pi*(f-f0))**2+2*(power/A)))

def cost(x, f,power, data):
    totalCost=0
    for i in range(len(f)):
        for j in range(len(power)):
            res=lor1(f[i],power[j],x[0],x[1],x[2], x[3])-data[j,i]
            totalCost+=(np.abs(res))**2
    return totalCost

linPow=10**(newpowers/10-3)  #converting in Watts
x0 =np.array([7.20972390e+06, 2.84620594e+06, 5.60628245e+09, 9.25e-20])

initialCost=cost(x0,frequencies, linPow,S11)
print('Initial cost = ', initialCost)
res1 = optimize.least_squares(cost,x0,bounds=([3.0e6,0.1e6,5.6e9,1e-22],[8.0e6,4.0e6,5.61e9, 10.0e-19]),verbose=2,args = (frequencies, linPow,S11))
print('final cost=',cost(res.x,frequencies, linPow,S11))
print(res1.x)
print('gamma is:',res1.x[0]/(2*np.pi*1e6),'(MHz), gammanr is:',res1.x[1]/(2*np.pi*1e6),'(MHz), mode frequency:',res1.x[2]/1e9,'(GHz) line attenuation:',res1.x[3])


#***********************************************************
#plotting functions
#***********************************************************


fig = plt.figure(1,figsize=(20,20))
plt.subplot(221)
for i in range(len(powers)):
    for j in range(len(frequencies)):
        plt.scatter(newFreq[i,j]/1e9, 20*np.log10(np.abs(S11[i,j])),c=cmap(17-i))
plt.xlabel('Frequency [GHz]', size=20)
```

```
plt.ylabel('Reflection Coefficient Magnitude |S11|', size=20)
plt.xlim(frequencies/1e9,frequencies/1e9)
plt.grid(True)
for i in range(len(powers)):
        plt.plot(moreFrequencies/1e9, 20*np.log10(np.abs(lor1(moreFrequencies, linPow[i], res1.x[0], res1.x[1], res1.x[2], res1.x[3]))),color=cmap(17-i))

plt.subplot(222)
for i in range(len(powers)):
    for j in range(len(frequencies)):
        plt.scatter(S11[i,j].real, S11[i,j].imag, c=cmap(17-i))
for i in range(len(powers)):
    plt.plot(lor(moreFrequencies, linPow[i], res1.x[0], res1.x[1], res1.x[2], res1.x[3]).real,lor(moreFrequencies[802:1216], linPow[i], res1.x[0], res1.x[1], res1.x[2], res1.x[3]).imag, color=cmap(17-i))
plt.xlim(-1.2,1.2)
plt.ylim(-1.2,1.2)

plt.xlabel("Real part (I)", size=20)
plt.ylabel("Imaginary part (Q)", size=20)

plt.subplot(223)
for i in range(len(powers)):
    for j in range(len(frequencies)):
        plt.scatter(newFreq[i,j]/1e9,np.angle(S11[i,j]), c=cmap(17-i))
plt.xlabel('Frequency (GHz)', size=20)
plt.ylabel('Reflection Coefficient Phase $\phi$ (S11) ', size=20)
plt.xlim(frequencies.min/1e9,frequencies.max/1e9)
plt.grid(True)
for i in range(len(powers)):
    plt.plot(moreFrequencies/1e9, np.angle(lor(moreFrequencies, linPow[i], res1.x[0], res1.x[0], res1.x[0], res1.x[0])),color=cmap(17-i))

cbar=fig.colorbar(
    cm.ScalarMappable(cmap=cmap, norm=norm),
    spacing='proportional',
    orientation='horizontal',
)
cbar.set_label('Driving Power (dBm)', size = 20)

plt.savefig('antisymfin.png')
```

**Listing C.1:** Python script used for fitting the data to the model of coherent scattering from artificial atom